Nano-materials for Novel Magneto-Rheological Liquids and Nano-fluids

by

Stephen V. Samouhos

B.S., Mechanical Engineering (2004)

Massachusetts Institute of Technology

Submitted to the Department of Mechanical Engineering
in Partial Fulfillment of Requirements for the Degree of
Master of Science in Mechanical Engineering

at the

Massachusetts Institute of Technology

June 2007



Signature of Author.....
Department of Mechanical Engineering
May 17, 2007

Certified by .....
Gareth H. McKinley
Professor of Mechanical Engineering
Thesis Supervisor

Accepted by.....
Lalit Anand
Chairman, Department Committee on Graduate Students

## Contents

# Acknowledgements

A great many thanks to all the individuals without whom this work could not have been done: Professor T.A. Hatton and his son Kent Hatton, for their collaboration on nanofluids, Jeremy Gordon for alumina nanoparticle TEM micrographs, Suraj Deshmukh for assistance in magneto-rheology, and the entire HML staff and students for their support. I would also like to offer very special thanks to Dr. Gareth McKinley, who has not only been a fantastic thesis advisor, but more importantly, a critical mentor in my education at MIT. Along those lines, I am also eternally grateful and indebted to the Hertz foundation, which not only financed the final year of master's study, but also graciously decided that I should continue my tenure at MIT for the PhD. Finally, I give thanks to my family for their support and love, and also to the Great Spirit which drives us all to persevere through adversity.

Here's to six years done at MIT...and onward to the next three or four.

# Figures

# 1.0 Introduction

## 1.1 Nanotechnology

Nanotechnology, in its many forms, has evolved as a forefront of the global scientific and technological frontier. Materials once disregarded as very small dust or particulate impurities twenty years ago, are today, the focus of intensely popularized investigation. New materials have been synthesized via nanometer precision engineering, and their resulting properties continue to defy the thermal, electrical, and mechanical limitations of conventional materials [1]. Even liquid suspensions of nano-particles yield tremendous enhancements in thermal and transport rates that still remain unexplained. Analogously, forty years ago the machining and synthesis of object features with nanometer dimensions and accuracy was a mere scientific interest. Today, that capability forms the core technical competency of the leading manufacturers of micro-processor electronics. The purpose of this thesis is to contribute to the field of nanotechnology through the synthesis of a novel nano-material, and to examine its utility in areas such as directed self-assembly and nanofluid enhanced mass transport.

The birth of nano philosophy is often credited to Dr. Richard Feynman, for his quintessential 1969 lecture entitled "There is Plenty of Room At The Bottom" [2]. In his lecture, Dr. Feynman lucidly contemplates a nano-machine capable of lifting a flea, and emphasizes the role of self-assembly in simplifying small scale fabrication. Ironically, nanotechnology as we know it had already been an area of ongoing research for many years before Dr. Feynman's prescient lecture. In 1964, Dr. Ronald Rosensweig, then at ExxonMobil Research, patented ferrofluids, a colloidal suspension of 10 nm magnetite particles [3]. Ferrofluids might be regarded as the first nanotechnology in the modern

sense of the word, despite the fact that colloid scientists since the early 1900's regularly dealt with systems having critical features at the nano-scale [3]. Ferrofluids indeed qualify for this distinguished title due to the ground-breaking balance of electromagnetic, thermal, chemical and size effects involved in their synthesis. The innovative engineering of ferrofluids, in conjunction with their commercial success proved that nanotechnology was not only possible, but also useful and valuable.

For the non-technical constituents of society, nanotechnology is often imbued with an aura of magic and high technology that all too often causes confusion regarding what nanotechnology really is. The reality is that nano-scale scientific research has persisted far longer than the general public realizes. In fact, the salient features of colloid science were developed long before the word nanotechnology became a cliché for modern materials research. The unique, and perhaps defining aspect of modern nano-scale research, are the anomalous phenomena observed in new materials that remain unreconciled with conventional physical theories. Equally important and definitive are the new design philosophies provoked by nano-scale engineering, which have found their way to influence numerous other engineering fields.

In the foregoing discussion, a nano-system or nanotechnology is qualified as any assembly containing at least one element that purposely contains or is influenced to nanometer accuracy. The physical and chemical underpinnings of the remarkable properties observed in most modern nano-materials are not well qualified. Current research is fueled by the tremendous technological implications of nano-systems, as well as the recognition that life itself has succeeded in harnessing nano-systems to its benefit.

Some sense of confidence in research can be taken from the fact that individual cells have successfully relied on nano-systems over the entire history of life.

### 1.2 Objectives and Scope

The work presented here is intended to contribute to the field of nanotechnology by introducing an innovative method for assembling magnetic carbon nanotubes, and exploring the utility of this new material in various applications. In particular, magnetic carbon nanotubes were specifically created and tested for use as microfluidic actuators, and the particulate constituents of magneto-rheological fluids. In addition, the composite was dispersed in water at low mass fractions, and the mass transport properties of this nanofluid, and several others were compared.

Research into the composite formation pathway has revealed novel methods for the spontaneous self-assembly between spherical and long cylindrical nanostructures. Likewise, the performance of a magnetorheological (MR) fluid based on magnetic carbon nanotubes (CNT) has been shown to possess qualities not found in analogous micron-size carbonyl Iron based MR fluids. Finally, the body of work on enhanced mass transport within nanofluids has revealed several salient features of the underlying physics behind the phenomena.

## 2.0 Magnetic Carbon Nanotubes

### 2.1 Introduction

Carbon nanotubes (CNT) have received a tremendous amount of attention due to their unique and highly desirable electrical, thermal and mechanical properties [1]. A variety of potential CNT applications exist, however technology development is in part hampered by the lack of effective means for manipulating these materials at very fine

scales [1]. Magnetic actuation of CNTs offers a potentially simple means for exerting this necessary control; however success is dependent on the ability to magnetize the CNT. Due to the absence of any natural CNT paramagnetism [1], their magnetization is only accomplished through hybridization with other magnetic materials, in particular cobalt, iron, nickel, and gadolinium. In this chapter, we review the variety of methods demonstrated to couple magnetic materials with CNTs, as well as the performance of the composite as a magnetorheological fluid.

There are three general approaches to creating a magnetic CNT composite; magnetic material can be encapsulated [4-9], incorporated within the walls [10-17], or deposited on the outer surface of the nanotube [18-20]. All three methods have been shown to impart some magnetic character to the nanotube. Each approach, however also modifies the nanotube in ways that may ultimately restrict the applications of the composite. Beyond these three material addition categories, methods can be further sub-divided into chemical and physical techniques that result in magnetic CNT composites. Physical additions include most of the processes in which material is encapsulated or imbibed by the nanotube, and as such, the majority of the molecular structure is kept intact. Wall embedding and outer surface decoration generally require, or induce some change in the wall or outer surface chemistry.

## 2.2 Filling techniques for composite formation

The earliest methods to create magnetic CNTs followed from the work of Ajayan and Iijima in 1993 [5], who successfully demonstrated the oxidative cleavage of CNT end caps and subsequent filling with non-magnetic liquid metals. Approaches derived from

the work of Ajayan and Iijima relied upon filling a tube with magnetically susceptible liquids. Initially this was accomplished by selectively oxidizing the ends of a fully formed nanotube, and then using capillary suction to imbibe a volume of liquid metal into the freshly opened tube [4, 5]. This two step process was executed by first depositing metallic nanoparticles onto a pristine nanotube outer surface, and then heating the composite material in air to beyond the melting temperature of the metal. The heating process both oxidized the tube end caps, as well as liquefied the metal. With the advent of techniques for creating vertically aligned, open ended CNTs [21], several other filling methods were also established.

In 2002, Bao et al. [6] showed that electrodeposition could be used to directly create continuous wires of cobalt within vertical nanotubes on an alumina template. Leonhardt et al [7] provides a review of analogous chemical vapor deposition techniques for creating metal nano-wires of iron, nickel, and cobalt within nanotubes. In a slightly different approach, Wu et al [9] demonstrated that an aqueous solution of Fe and Ni ions could be drawn into a CNT and, through wet chemistry, form Fe-Ni alloy nanoparticles within the CNT. Finally, Korneva at al [8] in 2005, also showed that an aqueous suspension of magnetic nanoparticles could be drawn by capillary suction, directly into an open ended nanotube. Subsequent evaporation of the solvent resulted in nanotubes loaded with magnetic nanoparticles. Most of these processes involve physical deposition, with minimal molecular modification of the CNT. In contrast, wall embedding and surface decoration generally involve significant chemical alterations of the CNT surface.

## 2.3 Wall embedding and surface decoration pathways

One of the earliest chemical additions of magnetic material to CNTs, performed by Lafdi et al. in 1996, was accomplished through cobalt doping of the graphite electrode used in arc-discharge CNT synthesis [12]. The CNTs subsequently produced from the doped electrode possessed walls that were infused with cobalt nanoparticles. Alternatively, Rao et al. [13] used pyrolitic synthesis, catalyzed by ferrocene, to form CNTs that had a magnetic nanoparticle embedded within the tube, at the catalyst anchoring point. Whereas Lafdi [12] was able to distribute the cobalt along the entire length of the tube, this latter approach could inherently only place a nanoparticle at one point. The methods employed by Rao were expanded in 2000 and 2001, by Liu et al [14, 15], and Zhang [17] respectively. Barnhart [16] provides a more complete review of the chemical and physical effects of metal atom inclusions within CNT walls, as well as the synthesis pathways leading to such composites.

In 2005, Bottini et al [22] showed that multi-walled CNTs could be covalently decorated with silica nanoparticles. The protocol required a long oxidation step to carboxylate the surface, after which various nanoparticle pre-cursor groups could be attached to the induced surface defects. Extended oxidation in concentrated nitric acid was necessary in order to stud the largely inert pristine CNT surface with reactive carboxylic groups. The protocol stems from an established method of using moderate etching periods in strong oxidizers to create nanotubes of uniform and predictable length, with minimal aberrations of the outer surface [23]. By dramatically extending the etch time, Bottini et al. increased the surface concentration of carboxyl group defects. As evidenced by TEM imaging of the composite material, the defect concentration was not sufficient to support total outer surface coverage by silica nanoparticles.

Georgakilas et al. [18] used a slight variation of this method in that same year, to stud the outer wall surface with magnetite. Utilizing pi-bond stacking, carboxylic defect groups on the CNT surface were bonded to a pyrene bearing magnetite nanoparticle, with an average diameter of 25 nm. As with other approaches that utilize surface defects, the coating process resulted in only partial coverage of the tube. Similar work was also presented in 2005 by Stoffelbach et al. [20] for decorating the outer surface with magnetite, and also in 2006 by Cao et al. [24]. Finally in 2005, Wu et al. [25] showed that by a similar process, nickel-iron alloy nanoparticles could be grown on the outer surface of the nanotube. In their protocol, the nanotube is again subjected to a prolonged oxidative bath in boiling nitric acid, which results in the formation of carboxylic surface defects. These imperfections provide the point of attachment for subsequent nanoparticle pre-cursors. In all cases, the density of surface defects is insufficient for complete coverage of the nanotubes by magnetic materials.

## 2.4 Design criteria for CNT-nanoparticle hybrids

External magnetic coatings offer the capability of magnetic actuation as well as continued CNT surface functionalization [24]. As the pristine CNT surface is chemically inert, localized magnetic surface groups, attached to the CNT, can provide points of attachment for materials that would otherwise not adhere to the CNT. Along those lines, the utility of such coatings, either in magnetic control or surface functionalization, is limited by the extent of surface coverage. One of the goals of our work is to develop magnetite surface coating techniques that result in complete coverage of the CNT.

The scientific interest in developing and reviewing the current techniques for nanotube-to-nanoparticle hybridization is ultimately driven by the needs of the design engineer who wishes to create precise multi-scale systems. As such, our interest in total surface coverage through techniques that do not modify the CNT surface may be completely superfluous to the needs of some technology developers.

Choosing amongst the existing art is dictated mostly by chemistry and application criteria of the hybrid materials. For a generic magnetic application, it may be sufficient to only rely upon the incorporation of the magnetic catalyst used during tube synthesis. This simple approach may prevail for long tubes that eventually only need one magnetic anchoring point. On the other hand, many synthesis processes are followed by a cleavage etch that would create tube segments with no magnetic character. Such situations can be resolved either by post-etch addition steps of either physical or chemical nature, or impregnation of the tube wall with magnetic particles during growth. Tube filling is another option that offers certain advantages to surface engineering, and can also be performed in situ with tube growth or post-cleavage etch. Applications that demand preservation of the outer tube surface chemistry should look to tube filling techniques. These same methods have generally also resulted in superior addition of magnetic character to the nanotubes.

Other than chemical and design criteria, production cost is certainly important for choosing a hybridization technique. Surface additions stem from the acid etch induced carboxylation of the CNT, which is a relatively low cost process step. The oxidation of the surface provides reaction sites that can be harnessed by numerous chemical means to deposit materials on the CNT surface. In general, these post-synthesis steps are easy to

apply, and can be performed by any laboratory. In contrast, the deposition techniques for in-situ tube filling during synthesis require a reaction chamber set up for the particular CVD process. Most CNT synthesis laboratories already have such utilities, but groups who purchase CNT might have to consider the added cost of that process in comparison to surface chemistry methods. The development of simple capillary suction methods for filling CNT represents a significant departure to this classical CVD paradigm, creating a low-cost, highly effective tube filling procedure. Our efforts to develop simple, analogous low cost surface encapsulation techniques that preserve the CNT outer surface chemistry would also provide additional options for the design engineer.

## 3.0 Total encapsulation of carbon nanotubes by magnetite

A surface preserving encapsulation procedure seemed feasible through non-covalent bonding between nano particles and tubes. In the absence of a chemical reaction or electrostatic bonding with surface defects, such a process could most likely proceed from the minimization of the van der Waals potential between the spherical nanoparticles and cylindrical nanotubes [26, 27]. Kirsch [27] has shown that for certain geometric and material parameter values, the van der Waals attraction is greatest between a sphere and cylinder than for either species to a neighbor of its own kind. In reality, minimal surface defects always arise from the brief oxidative bath, as prescribed by Liu et al [23], used to cut CNTs to a desired length. In the case of defects, electrostatic interactions introduce random points of attachment that do not usually support full tube encapsulation. Not having to depend on defect anchor points, the desired non-covalent bonding mechanism may result in full surface coverage.

## 3.1 Method for coating of carbon nanotubes with magnetite

The CNTs used to explore this technique were acquired from NanoLabs (Newton, MA), who carried out the ferrocene pyrolitic synthesis of 30 nm outer diameter stock multi-walled CNTs. The synthesis was followed by a three hour concentrated nitric acid reflux etch, performed by NanoLabs, that cleaved the stock material into 5 μm long, open ended segments. TEM inspection and observed low aqueous miscibility confirmed that the outer tube surface acquired minimal carboxylation defects during the etch. No further oxidation steps or chemical treatments were employed after the etching bath.

To explore the non-covalent bonding mechanism, 10 ml of an organic ferrofluid (EFH-1, Ferrotec, Nashua, NH.), and a water-based ferrofluid (MSG-W11, Ferrotec, Nashua, NH.) were added drop wise to separate Petri dishes each containing 1.0 g dry CNT samples. Both ferrofluids were constituted of 10 nm magnetite nanoparticles, coated with an appropriate surfactant, and loaded to 6 % volume fraction in their respective carrier liquid. As expected from prior miscibility experiments, the CNTs exhibited strong hydrophobicity, and the aqueous ferrofluid did not spontaneously wet the nanotubes. Conversely, the CNTs were immediately wet by the organic ferrofluid. The contents of each dish were mixed with a glass rod, and then washed with excess ethanol into 45 ml plastic tubes, without any sonication. The tubes were shaken vigorously to further mix the materials. The tube contents were separately washed with excess ethanol, and then excess kerosene, through a vacuum filtration system. In both cases, a reddish brown filtrate ensued, with a dark pink colored solid remaining on the filter paper. The filtrate was discarded, and the filter paper contents were washed with ethanol back into glass vials for storage.

## 3.2 Visualization of novel CNT-magnetite hybrids

Figures 1 and 2 show TEM micrographs (100kV acceleration potential) of both the oil and water based ferrofluid reaction products in ethanol, following three hours of sonication.

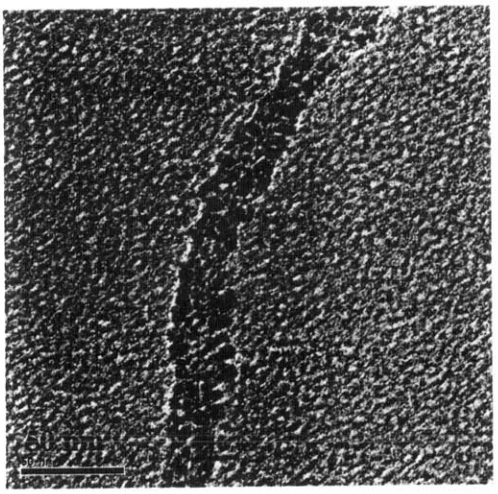

**Fig 1. TEM of organic ferrofluid nanoparticles bound to a CNT**

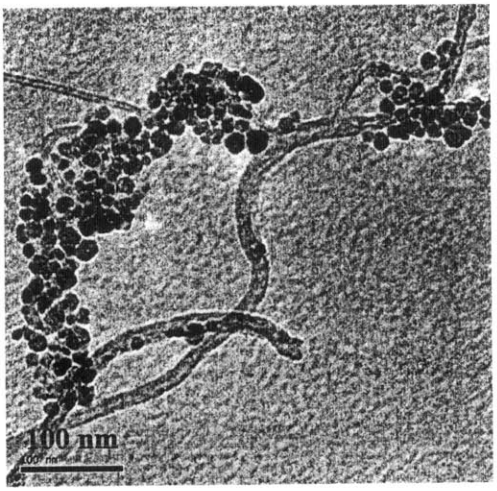


**Fig 2. TEM of aqueous ferrofluid nanoparticles excluding CNTs**

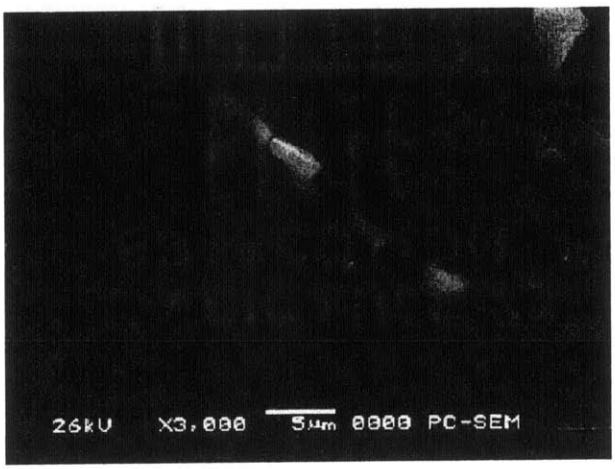


**Fig 3. SEM of bamboo structured ferrofluid nanoparticle-CNT composite**

The magnetite particle and CNT diameters can be estimated from the TEM images as approximately 10 and 30 nm, respectively. These values match the quoted sizes given by the manufacturers. The initial hydrophobic interaction and poor miscibility

between aqueous ferrofluid and CNT may have foretold the results shown in figure 2. The aqueous ferrofluid particles generally agglomerate with themselves, and occasionally attach to the surface of the CNT. The sporadic surface deposition may be attributed to the presence of a low concentration of carboxyl surface defects initiated by the oxidation etch. These defects facilitate electrostatic bonding with the charged surfactant group of the aqueous ferrofluid magnetite particle. In stark contrast, the organic ferrofluid appears to have fully coated the entire CNT. This image is reproduced in several other TEM micrographs, and indicates that our process results in complete CNT coating by magnetite nanoparticles. Based on the conditions of the experiments, non covalent bonding due to van der Waals attraction or surfactant-CNT surface affinity has produced hybrids with high surface coverage. Moreover, the composite products of the organic reaction can be stabilized by a surfactant such as CTAB, or SDS and show satisfactory sedimentation stability in water, up to 0.1 % volume fraction. The composite material alone shows higher stability against sedimentation in organic media without the aid of any surfactants.

The SEM image in figure 3 shows a larger object, comprised of several of these magnetite/CNT composites. Considering the dimensions of an individual strand, as shown in the TEM, this SEM suggests that several composite strands can braid or envelope each other to form a bamboo structured micron-sized cylinder.

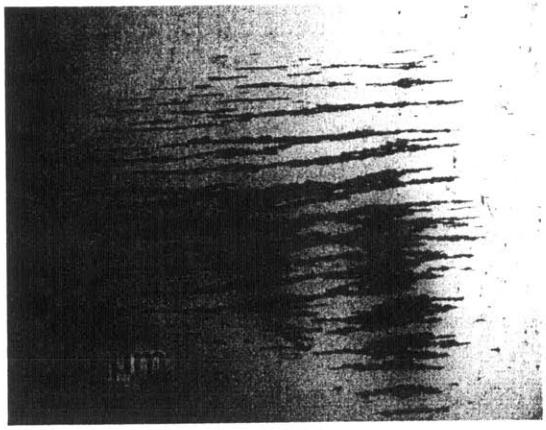

**Fig 4. Micrograph of composite filaments aligned by 20 mT field applied parallel to the page**

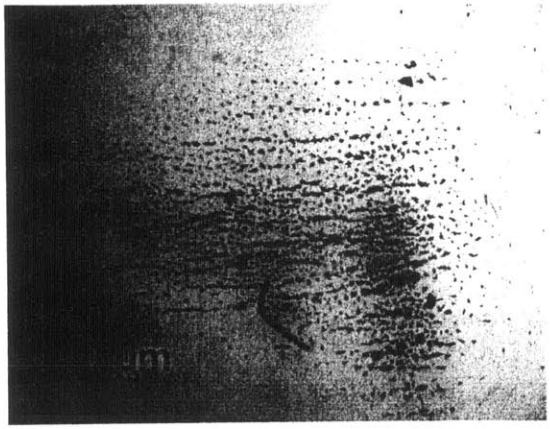

**Fig 5. Micrograph of composite filaments aligned by 20 mT field applied normal to the page**

Figures 4 and 5 present static snapshots of the alignment of these braided composite strands to a lateral and normal induction field of 20 mT. The composite is clearly manipulated by the field to remain parallel with the field lines. There is likely a critical size, or number of strands per cylindrical agglomerate, that is indicative of steric and perhaps magnetic interactions between individual composite tubes. This saturation size is supported by the observation that figures 3, 4, and 5 shows a large number of these agglomerate braids all with roughly 2.5 μm diameter and 20-30 μm in length. The manufacturer's quoted dimensions for the nanotubes are 30 nm diameter, by 5-20 μm long; considering that a magnetic coat increases the outer diameter to 60 nm, these braided agglomerates are comprised of roughly 40-50 individual strands.

Correa-Duarte et al [28] also achieved complete coverage with magnetite through a non-covalent bonding mechanism based on polymer wrapping and layer-by-layer (LbL) electrostatic self-assembly. Poly(sodium 4-styrene sulfonate) chains were driven to wrap around the CNT via hydrophobic interactions, thereby encapsulating the CNT in a negatively charged polymer coat. The polymer surface charges then acted as anchors for the subsequent deposition of magnetic nanoparticles via LbL, and total surface coverage

ensued. Pu and Jiang [29] also attempted surface coating via extended oxidation to create carboxyl defects on the CNT surface. These defects served as nucleation sites in the subsequent chemical synthesis of magnetite from ferrous and ferric salts. This approach resulted in the formation of a 10 nm thick shell of magnetite surrounding the CNT. TEM analysis, however, shows a shell that only covers certain portions of the CNT, as opposed to the total surface coverage wrought by our non-covalent bonding. In contrast to other carboxylation based methods, however, which result in only particle decoration of the CNT surface, Pu and Jiang were successful in producing continuous magnetite shells on the CNT surface, albeit without total surface coverage.

## 3.3 Sedimentation stability of CNT-nanoparticle dispersions

Part of the motivation for creating a CNT/magnetite composite stems from the goal of creating a magneto-rheological (MR) fluid with increased sedimentation stability. The density of the magnetite/CNT composite formed by our protocol was approximately 1.8 g/cm$^3$, which is less than a quarter of that of Carbonyl Iron, $Fe(CO)_5$, a material commonly used to form particles for MR fluids. By comparing the buoyancy of a particle against the viscous drag experienced as it falls within a fluid, the sedimentation velocity may be expressed by [30]

$$V_o = {2(\rho_s - \rho_f) g a^2} \Big/ {9\eta} \qquad (1)$$

where $V_o$ is the sedimentation velocity, $\rho_s$ and $\rho_f$ are the particle and fluid densities respectively, $a$ is the particle radius, $\eta$ is the viscosity of the fluid, and $g$ is the gravitational acceleration. The difference in density between a 1 μm diameter

(hydrodynamic) CNT/$Fe_3O_4$ composite particle and 1 μm diameter iron oxide particle should result in a seventeen fold reduction in the sedimentation velocity of the composite as compared to iron oxide particles, dispersed in water. Moreover, at high enough volume fractions (above 10%), the elongated cylindrical shape of the braided composite particles should also provide sedimentation stability via the formation of a percolated network. Pu and Jiang created a composite with similar density and cylindrical geometry, and found that the sedimentation stability of their CNT/magnetite composites dispersed in water increased with increasing volume fraction. Their result was attributed to the formation of a percolated support structure that prevented sedimentation.

The sedimentation stability of MR fluids has been a continual problem in the development of MR fluid technology [31, 32]. The combination of hollow, lighter weight CNTs with super-paramagnetic [3] magnetite nanoparticles can lead to a unique MR fluid that does not suffer from sedimentation limitations. The improved stability may be realized through both the use of composite materials with lower mass densities as well as particle geometries such as elongated cylinders that form percolated networks. The success of these novel MR fluids, however is contingent upon the preservation of the field dependent critical stress and modulus seen in conventional iron oxide and carbonyl iron based MR fluids [33-36].

## 4.0 Magnetorheological fluids and ferrofluids

Conventional MR fluids date back to their discovery in 1948 by Rabinow [37]. They followed as a natural magnetic analog to the electro-rheological fluid patented by

Winslow [38] in 1947. Depending on the desired effect, the fluids are surfactant stabilized suspensions of either dielectric, or paramagnetic micron sized particles, dispersed in a carrier liquid. Ferrofluids [3] are another family of magnetically active liquids, whose surfactant stabilized particle constituents are 10-20 nm in size, and consist of single domain, permanently magnetized magnetite. Consequently, the response of a ferrofluid to a magnetic field is markedly different from that of an MR fluid [3].

## 4.1 The physics of MR fluids and ferrofluids

MR fluids consisting of 1 μm carbonyl iron particles, at 30% volume fraction, have a maximum critical stress in the range of 10 - 100 kPa for applied induction fields near 0.2 Tesla [33, 35]. The zero shear rate viscosity, which persists until the critical stress is surpassed, may exceed 1 MPa s. In contrast, the ER effect provides critical stresses typically no greater than 1 kPa, at fields near 1kV/mm. This performance limitation is imposed by impurities within the carrier liquid, oxide layers on the dispersed particles, and the dielectric breakdown voltage of the ER suspension carrier fluid. Analogously, the MR effect is limited by the saturation magnetization of the constituent magnetic material. Coating techniques similar to the surface decoration methods we have discussed above have also been used to overcome these ER limitations by creating a high dielectric constant suspension of Urea coated Barium Titanate Oxalate nanoparticles, suspended in Silicone Oil. The resulting ER fluid exhibits an un-precedented 130 kPa yield stress without dielectric breakdown [39].

MR fluids show an apparent viscosity that is dependent on the applied magnetic field, shear stress, particle volume fraction and carrier viscosity [36]. With the

application of a magnetic field at values below the saturation value for the paramagnetic material, a magnetic dipole results according to

$$\vec{m} = \frac{4}{3}\pi a^3 \mu_0 \chi \vec{H} \qquad (2)$$

where $\vec{m}$ is the particle polarization, $a$ and $\chi$ are the particle diameter and dimensionless susceptibility respectively, and $\mu_o$ and $H$ are the free space permeability and applied field respectively [36]. The induced dipoles interact with one another to form particulate aggregates whose size grow with the square root of elapsed time (measured from the onset of the magnetic field) [40]. The particle aggregates grow into longer bundles, and eventually into threads extending along the magnetic field lines. Eventually, these threads coarsen due to lateral attraction and form crystalline pillars of magnetized particles [35, 41]. The formation of aggregates is opposed by Brownian dispersion, and as such the potential for field induced aggregation versus Brownian dispersion can be expressed in terms of a governing dimensionless parameter, often referred to as a coupling coefficient

$$\lambda = \frac{\pi(\mu_o \chi H)^2 a^3}{18 k_B T} \qquad (3)$$

where the parameters T and $k_B$ are the temperature and Boltzmann constants, respectively [36]. For the case $\lambda \gg 1$, aggregation is highly favored, and at $\lambda \ll 1$, dispersion is favored. The case of small $\lambda$ is used as a design parameter for the creation of ferrofluids, or stable dispersions of super-paramagnetic nanoparticles in organic and aqueous carriers [3], whereas $\lambda \gg 1$ commonly results in MR fluids [36]. Due to the presence of permanent magnetic material within ferrofluids, as opposed to the paramagnetic material typically found in MR fluids, the aggregation parameter for

ferrofluids is calculated according to where $\mu_o M_s$ is the remnant magnetization of the particle [3].

$$\lambda = \frac{\mu_o M_s H \pi a^3}{6 k_B T} \tag{4}$$

The re-organization of the MR fluid microstructure due to shearing comes at the interplay of hydrodynamic and magnetic forces. The ratio of these interactions within an MR fluid forms a second dimensionless parameter known as the Mason number [33, 36, 42] that governs the break up of magnetic microstructure due to shear

$$Ma = \frac{9\sigma}{2(\mu_o \chi H)^2} \tag{5}$$

where the parameter $\sigma$ is the applied shear stress. Alternate governing dimensionless parameters include a Peclet number (dimensionless time) formed by the ratio of shear rate to the Brownian diffusion time as well as the particle volume fraction. The Mason number (eqn. 5), Peclet number, and coupling coefficient (eqns. 3,4) are inter-related via Pe ~ Ma×λ. An analogous ferrofluids Mason number can be constructed by the ratio of the applicable Peclet and aggregation parameters. In contrast to MR fluids, the field-independent rheological properties of ferrofluids reduce the utility of a ferrofluids Mason number.

At low applied fields, where saturation effects are completely absent, the Maxwell magnetostatic stress accurately predicts that the yield stress within MR fluids is proportional to the square of the applied magnetic field [34]. As the field intensity is increased such that saturation begins to occur at the surface of the dipolar particles, the critical stress ($\sigma_c$) transitions to a weaker dependence on the applied field, and the elastic modulus (G) grows linearly with the applied field. Ginder et al. [34] were able to model

this saturation effect and found analytical models for the critical stress and elastic modulus that accurately predicted the data for carbonyl iron MR fluids [34, 43].

$$\sigma_c = \sqrt{6}\phi\mu_o M_s^{1/2} H^{3/2} \tag{6}$$

$$G = 3\phi\mu_o M_s H \tag{7}$$

where $\phi$ is the volume fraction. This saturation effect is amplified by the increased field density within the small gap between particles undergoing aggregation. At still higher fields that exceed the physical saturation magnetization of the magnetic material, the response becomes field independent and limited only by the saturation of the material and particle volume fraction.

$$\sigma_c^{sat} = 0.086\phi\mu_o M_s^2 \tag{8}$$

$$G^{sat} = 0.3\phi\mu_o M_s^2 \tag{9}$$

In stark contrast to the performance of MR fluids, ferrofluids do not display a dramatic change in viscosity as a function of applied field [44]. There is a marginal change in fluid viscosity at very small shear rates with an applied field, but at high shear rates or strong applied fields, the apparent viscosity does not change. Moreover, an exceedingly small if any critical stress exists for the ferrofluid irrespective of the applied field [3]. This difference in response between these two magnetically active fluids results from the typical magnitudes of $\lambda$ parameter previously defined in equations (3) and (4) for MR and ferrofluids respectively; for $\lambda \ll 1$ in equation (4), as is the case with ferrofluids, persistent filamentous or tertiary aggregates can not form even in strong magnetic fields. In the absence of such a microstructure, the ferrofluid does not exhibit a critical stress induced by a magnetic field [3]. A field dependent viscosity is observed in ferrofluids, but is attributed to the torque of a rotating magnetic field on the nanoparticles

themselves [45]. Represented as an un-symmetric stress tensor within the continuum description of the ferrofluid, so called negative or zero fluid viscosities can be observed, and are a result of the rotating magnetic field [46, 47]. In the absence of a magnetic field, the viscosity shows some shear thinning at high shear rates. The apparent viscosity is generally considered to be volume fraction dependent according to the Einstein relation in the dilute suspension limit [3]

$$\frac{\eta}{\eta_o} = 1 + \frac{5}{2}\phi \qquad (10)$$

where $\eta_o$ is the nominal carrier viscosity, and $\eta$ is the apparent viscosity of the suspension. Higher order terms can be included to account for volume fractions beyond the dilute limit [3]. Whereas MR fluids typically have volume fractions exceeding 30% , commercial ferrofluids do not extend beyond 10%.

## 4.2 The effects of combining MR fluids and ferrofluids

Several approaches have been taken to improve the magnitude and speed of MR fluid response [31, 48]. Of note are methods for increasing the field-on viscosity to attain a more solid-like response below the critical stress [49], as well as methods for decreasing the response time, or lag between fluctuating field and particle tracking [50], and finally increasing the critical stress via reducing the limitations imposed by magnetic saturation [51]. These methods tend to employ mixtures of both nano and micro sized magnetic material, which often has the additional benefit of increasing sedimentation stability [50-52].

Popplewell et al. [49] explored inverse MR fluids in 1995 to achieve some of these improvements. A commercial ferrofluid was used as the carrier liquid, with a

suspension of 1 micron glass beads. It was found that application of a magnetic field induced the formation of rudimentary glass bead columnar structures, and a typical MR response ensued, albeit with reduced critical stress. For bead volume fractions at 60%, and 36 mT induction field, the critical stress was about $\sigma_c \sim 20$ Pa, with an ensuing viscosity of 0.4 Pa s. Experiments were repeated with aluminum and iron parallel plates, and the iron geometry was found to produce a greater divergence in the zero shear rate towards infinite. It was proposed that the lack of magnetic attraction between the aluminum geometry and ferrofluid provided a mechanism for slip and hence a reduction in the zero-shear rate viscosity. Owing to the paramagnetic nature of both the ferrofluid and iron, and the diamagnetic nature of aluminum, the ferrofluid magnetically adheres to the iron plate, and provides a more accurate measurement of the viscoplastic solid-like creep response below yield.

The limitations due to saturation and sedimentation were both explored by Chin et al [51] in 2001. Building on prior work by Phule and Ginder [53] and Chen et al [54], MR fluids comprised of micron sized carbonyl particles, interspersed with cylindrical nanoparticles of Co-$\gamma$-$Fe_2O_3$ and $CrO_2$, were created and shown to have a dramatically increased sedimentation stability and saturation critical stress. The critical stress enhancement was found to be a strong function of applied magnetic field, with an increase of 30% in a 64 mT field, versus less than 5% for a 16 mT field. This enhancement phenomenon was attributed to a shielding effect owing to the greater saturation magnetization found within cobalt materials as compared to carbonyl iron.

As was shown by Ginder et al [34], saturation begins to limit the MR effect once the MR particles begin to experience localized saturation due to the increased field

density within the thin gap between magnetic particles. By interspersing the gap with nanoparticles of higher magnetic saturation (cobalt materials can have nearly double the saturation of purely ferromagnetic species), the increasing field density can be distributed between MR particles and cobalt particles, where the greater saturation of the cobalt can shield the MR particles from reaching saturation. This shielding effect proposed by Ginder is less pronounced at lower fields, where neither the nanoparticles nor MR particles are near saturation. However, as the field strength increases, the saturation mitigated by the nanoparticles results in a greater interaction between MR particles, and hence stronger columnar structures and increased critical stress.

Purely nanoparticle based MR fluids have also been explored independently by Kormann et al. [50]. Ferrite nanoparticle suspensions of roughly 30 nm diameter, and 60 % mass fraction, were shown to behave as MR fluids. This is in stark contrast to ferrofluids with particle sizes only half the diameter, and volume fractions less than a sixth that value. At zero applied field there was only a slight critical stress owing to a percolated network, but as the field was increased to 0.4 T, the critical stress rose almost to $\sigma_c \sim 4000$ Pa. The direction of the applied magnetic field in 100 Hz AC experiments was not observed to affect the critical stress, which suggests that the switching speed of the nano MR fluid is less than 5 ms, and there was no lag between the AC induction field and particle tracking of that field.

Poddar et al [52] provides a complete comparison of conventional (micron sized), nanoparticle, and hybrid particle MR fluids. The essential results are that MR fluids with micron sized particles exhibit superior critical stress, but poor sedimentation stability. Conversely, nano MR fluids are found to have a much smaller critical stress, but much

improved sedimentation stability. Hybrid systems offer a mix of both desirable qualities, where the actual performance may be tuned via the use of appropriate materials and sizes for the micro and nano particles. The performance of an MR fluid formed by dispersion of our own magnetite/CNT composite in silicon oil differs from both the traditional MR and ferrofluid responses.

## 5.0 Magnetorheology of novel CNT-nanoparticle suspensions

### 5.1 MR response of the FFCNT suspension

The ferrofluid-CNT (FFCNT) composite was dispersed in silicon oil (100 cSt PDMS oil, Siloxane terminated, Gelest inc, PA) at 5%, 10% and 20% w/w fractions. Creep tests were performed in a parallel plate geometry, with a 40 mm anodized steel rotating plate, on an AR2000N rheometer (TA Instruments). A custom designed MR fixture was employed to produce a uniform magnetic field normal to the sample [55]

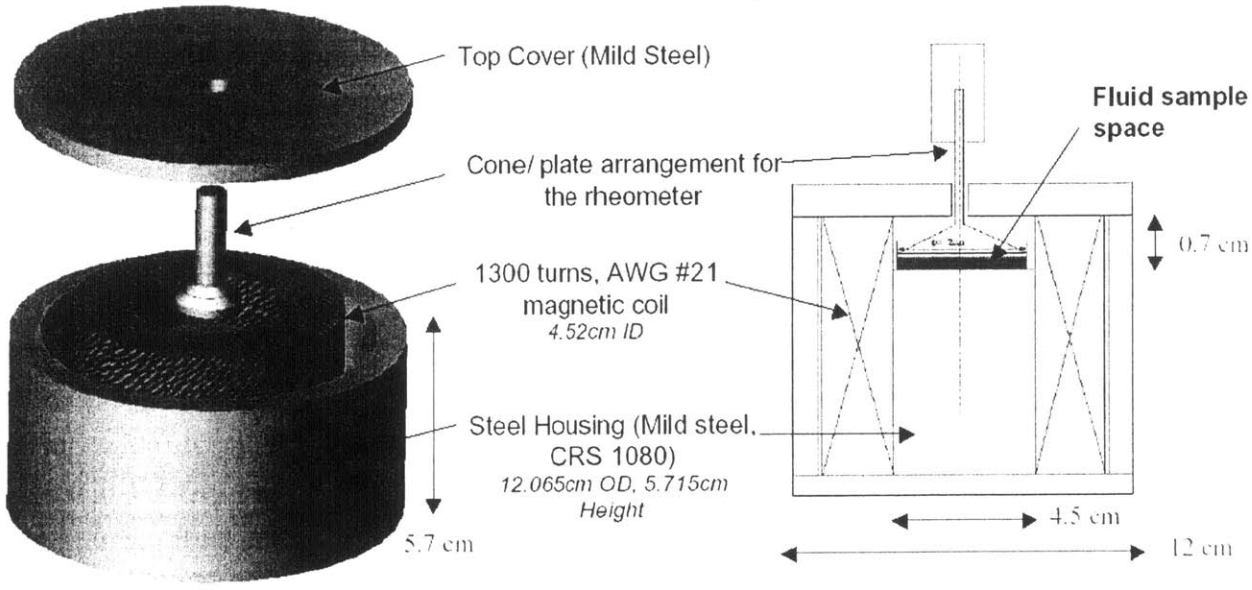


**Fig 6. Custom designed MR fixture for AR2000 Rheometer**

Several creep experiments at constant shear stress were performed for each of three different stresses and volume fractions, and four different induction field strengths.

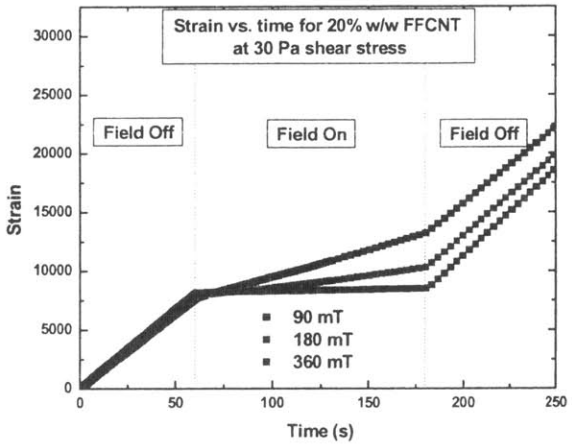


**Fig 7. Strain vs. time for 20% w/w FFCNT, at 30 Pa shear stress, and three different induction**

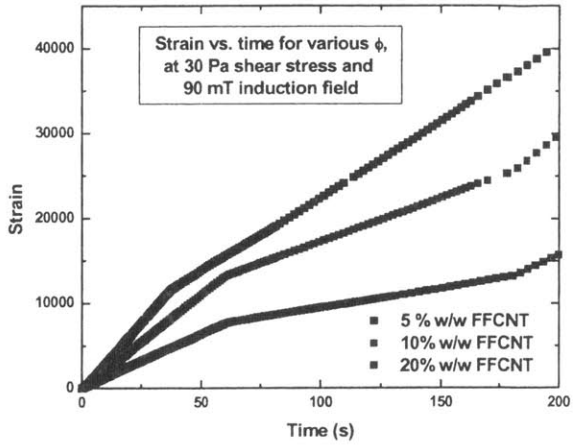


**Fig 8. Strain vs. time for a 30 Pa shear stress and 90 mT induction field, at thee different mass fractions**

After each experiment, the sample was examined to ensure that the particles had not settled out of the suspension. The experiments were all conducted at 25 °C, and maintained by a Peltier element below the MR fixture and a small fan that was used to intermittently cool the induction field coils after prolonged use. Figure 7 shows a consistent viscosity between samples within the field off regions. As expected, the rate of strain changes for each sample as a function of applied induction field, with the highest field strength resulting in the most diminished strain rate. Once the field is removed, the strain rate returns to its pre-field value, regardless of the applied field intensity. These experiments were also repeated with other volume fractions of FFCNT composite. Figure 8 shows the viscosity shift as a function of increasing volume fractions. The greatest strain rate is observed at the lowest volume fraction, as is expected. The shift in zero field strain rate also appears to vary linearly with increasing volume fraction.

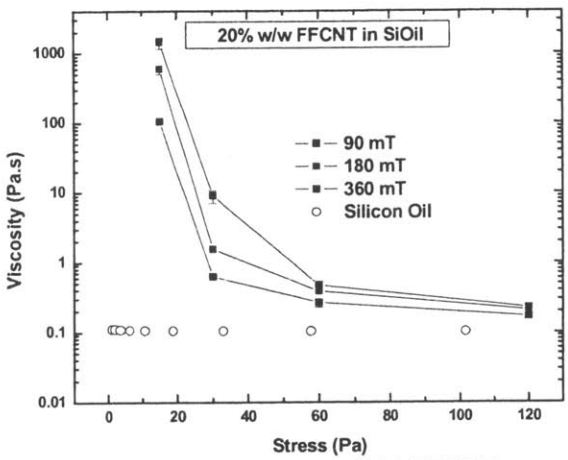


**Fig 9. Viscosity vs. Stress for 20% FFCNT at three induction fields**

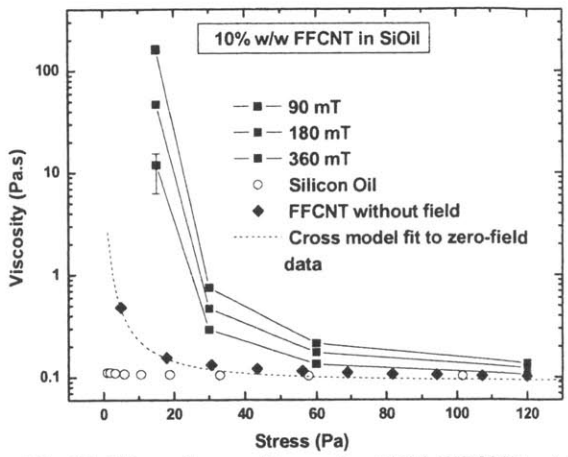


**Fig 10. Viscosity vs. Stress for 10% FFCNT at four different field strengths, with a Cross model fitting to the zero field data**

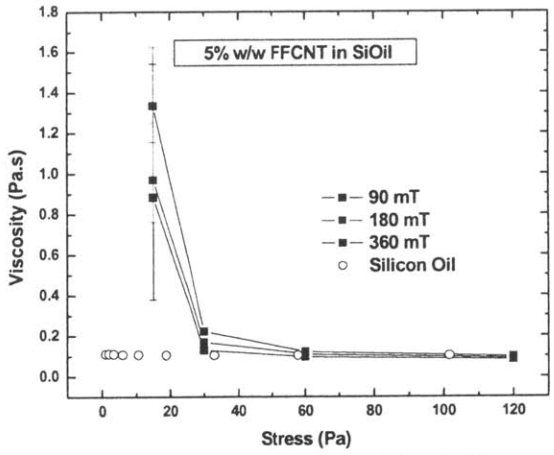


**Fig 11. Viscosity vs. Stress for 5% FFCNT at three induction fields**

The shear rates for these creep experiments can be determined and used to evaluate the stead state shear viscosity $\eta(\phi,B,\sigma)$ as shown in figs. 9-11. Apparently irrespective of applied field or particle mass fraction, these figures show that the FFCNT composite exhibits a critical stress between 20 and 30 Pa. As the stress is progressively decreased the viscosity diverges and the fluids become increasingly solid-like. Continued shear thinning, albeit at a lesser rate, is expected as shear stress increases, until the carrier viscosity is ultimately attained. As evidenced by the data, the rate of approach to this

minimum is a function of both applied field and mass fraction. The 5% fraction reached the carrier viscosity (0.1 Pa s) by 60 Pa for all field strengths. The 20% and 10% samples exhibit a more gradual asymptotic approach at stresses $\sigma > 60$ Pa. Beyond 60 Pa, for all mass fractions, and applied induction fields, the test samples approached an infinite shear viscosity nearly equivalent to the carrier viscosity.

## 5.2 Model for the MR response of the FFCNT suspension

To model our CNT/$Fe_3O_4$ composite, it is assumed that the magnetic material lies within an external cylindrical coating of thickness ε, and is composed of randomly oriented super-paramagnetic particles. This formation is a unique departure from the conventional carbonyl iron MR fluid particle, because the material composition allows for self-interaction in the absence of an applied external magnetic field. As such, the FFCNT may be considered to possess a combination of ferrofluid and MR particle properties. Due to the magnetic character of the hybrid, the aggregation parameter for our composite is likely to follow the ferrofluids model, as developed by Rosensweig [3], with an adjustment for the cylindrical shell geometry [36]. The greatest possible self-interaction field between two FFCNT cylinders would be 0.56 T, in the limit of favorable alignment of the super-paramagnetic particles whose remnance magnetization is 0.56 T. Equation 4 for the ferrofluids aggregation parameter can be modified for a cylindrical super-paramagnetic shell of thickness $\varepsilon$, tube radius $a$, and composite length $L$ and becomes

$$\lambda_m = \frac{\mu_o MH\left[(\varepsilon + a)^2 - a^2\right]L\pi}{12k_B T\left(\ln\left(\frac{L}{2\varepsilon + 2a}\right) - 0.8\right)} \qquad (11)$$

Calculating the value of this parameter for our magnetite – CNT composite gives $\lambda \cong 630$ and the self interaction potential in the absence of external fields is therefore much closer to that seen in conventional MR fluids during actuation by an applied field. Based on this calculation, magnetic aggregation in the absence of an external field could be a partial explanation for the existence of micron-sized cylinders composed of multiple FFCNT threads. In MR fluids, $\lambda \gg 1$ leads to spontaneous agglomeration and sample spanning structures upon application of an external field, and this leads to solidification of the entire fluid volume. In contrast, FFCNT aggregation induced by self-interaction appears to terminate after the combination of a sufficient number of individual threads.

The response to the imposed fields and shear stresses can also be quantified by considering an appropriate Mason number for each experimental data point. The Mason number as defined in equation 6 is not correctly posed for a field responsive fluid composed of cylindrical, super-paramagnetic components such as these FFCNT composites. Relying upon the relationship between Peclet and Mason numbers, and the coupling coefficient as defined in equation 11, a modified Mason number better suited for the FFCNT can be calculated in the form

$$Ma = \frac{3\sigma(2\varepsilon + 2a)^2 \ln\left[\left(\frac{L}{2\varepsilon + 2a}\right) - 0.8\right]}{\mu_o MH\left[(\varepsilon + a)^2 - a^2\right]} \qquad (12)$$

Equation 12 demonstrates the appropriate interplay of hydrodynamic forces and those arising from the applied magnetic field, modified for the cylindrical geometry and super-paramagnetic material. The calculated Mason number for these flows varies from 0.29 for a shear stress of 120 Pa shear stress and an induction field of 90 mT, to 0.009 for $\sigma$ = 15 Pa and $\mu_o H$ = 360 mT. These values represent the two extremes in the range of

Mason numbers for the experiments shown in figs. 9-11. As expected, the highest values coincide with a Newtonian fluid-like response as observed when the fluid approaches an infinite shear-rate viscosity, and the lowest values coincide with the viscoplastic response observed at low shear stresses.

The fluid viscosities both below and above the critical stress, show a significant dependency on the magnitude of applied field and particle mass fraction. Likewise, the rate of shear thinning in the critical stress zone varies by orders of magnitude between different mass fractions.

The shear thinning behavior of CNT dispersions was also studied by Yang et al. [56]. Critical stresses for CNT volume fraction samples ranging from 0.04% to 0.42%, dispersed in low viscosity (4 – 6 cSt) poly-olefins, ranged from 0.04 Pa to 0.13 Pa respectively. Flow experiments were performed, and the shear thinning behavior was fitted to the Cross model

$$\frac{\eta-\eta_\infty}{\eta_o-\eta_\infty}=\frac{1}{1+b\dot{\gamma}^P} \qquad (13)$$

with values for $P$ ranging from 0.560 to 0.772 in CNT suspensions. This expression also accurately describes the present zero-field rheological data as shown in fig. 10. The range of data available preclude accurate determination of $\eta_o$, however the values of $b$ = 205 and $P$ = 0.725 are consistent with [54]. Further experimentation with our FFCNT suspensions demonstrated that a critical stress range still persists between 6 and 12 Pa, even in the absence of a magnetic field.

Given the magnitude of the critical stress, and its persistence from 5% to 20% mass fractions, the critical stress appears to arise due to percolation of the cylindrical FFCNT composite. The range is amplified from previously mentioned critical stress

based on particle percolation due to the addition of super-paramagnetic material that provides an additional strengthening interaction amongst the network members. The lack of a stronger field dependence in the critical stress is expected for a ferrofluids but not for an MR fluid in which the response is dominated by field-induced particle chaining. Conversely, the dependence of the zero shear-rate and infinite shear-rate viscosities on the induction field are expected for an MR fluid, but not found in a ferrofluid. It seems that this unique FFCNT composite exhibits attributes from both constituents, displaying a critical stress derived from a magnetically strengthened percolation network as well as field and mass fraction dependent zero and infinite shear viscosities.

## 6.0 Nanofluid transport

Nanoparticle suspensions (Nanofluids) have been observed to exhibit convective and diffusive thermal [57] and mass transport [58] rates that exceed those of their respective carrier liquids by nearly an order of magnitude. Experiments repeated in various laboratories, however, have not universally supported these claims, leaving uncertainty surrounding the physical versus analytical origins of such dramatic enhanced performance measurements [59-61]. The inability of accepted conventional multi-phase system models to predict or explain such enhancement phenomena further necessitates continued research under precision experimental conditions [62].

Through our study of nanofluid enhanced diffusive mass transport we have attempted to isolate the effects of Brownian motion [63] on diffusive transport within nanofluids. Brownian motion effects are a common feature amongst several competing nanofluid theories posed over the last decade [57, 60, 64]. One of the intended goals of

this work is to test the validity of a Brownian motion based theory. A binary diffusion experiment was carefully selected for this purpose and automated in order to yield large data volumes that could provide robust conclusive evidence regarding enhanced diffusion within nanofluids. Moreover, the experimental setup was carefully constructed to yield highly reproducible results that were solely attributed to concentration gradient driven diffusion.

Our interests in the application of nanofluid enhanced mass transport to industrial oxygenation systems also prompted additional oxygen dissolution experiments within a nitrogen sparged vessel [58]. These experiments provided bulk measurements for the rate of oxygen uptake within nanofluids. Bulk convective transport experiments were repeated under conditions that probed the relative magnitudes of the transport resistances attributed to the gas and liquid side boundary layers, as well as the interface between these phases. Surface tension measurements, in conjunction with the sparged reactor data, were included to quantify the importance of the interfacial transport resistance. Finally, the combination of sparged reactor data, surface tension measurements, and binary diffusion measurements provided a superior insight to the true role of nanoparticles in the observed enhanced mass transport within nanofluids. While nanofluid enhanced mass transport is a relatively young problem, the classical analogy between heat and mass transport may enable this study to contribute to our understanding of nanofluid enhanced heat transfer, which has eluded scientists for the better part of a decade.

## 6.1 Nanofluids and enhanced mass transport

Nanofluids have been suggested as a novel three phase reactor system [58, 65], with several distinct features that contrast a conventional fluidized bed. Classical fluidized or slurry reactor beds are characterized by solid particles no smaller than 1 micron, usually loaded beyond 30% w/w, that are maintained in suspension either by continuous mechanical agitation or gas sparging [66]. In such reactors, larger particles are preferable since transport and reaction rate enhancement are attributed to the ability of the slurry to reduce gas hold up and bubble coalescence, and fortify turbulent mixing. The particle surface chemistry and surface area also play a catalytic role during the reaction of different species, and surface adsorption of molecules [67, 68]. In general, fluidized beds can enhance transport by an order of magnitude, albeit with the additional material costs and practical flow limitations imposed by high particle loading and large particle size [66, 69].

Fluidized beds themselves also tend to be large structures, immobilized by their ancillary equipment such as pumps and containment systems. The superficial liquid velocity as well as gas flow rate within the chamber must be carefully limited in order to prevent bed dispersion [70]. Work done so far on nanofluid mass transport has shown enhancement factors on the same order as those observed in fluidized beds, but without the physical limitations found in the latter [58].

In contrast to slurry bed reactors, nanofluids are an inherently stable suspension that possess a bulk viscosity nearly identical to their pure carrier, and do not suffer from conduit flow limitations imposed by particle aggregate clogging, or bed dispersion in the reactor vessel. Moreover, a nanofluid reactor loaded with a 1% w/w suspension of 100

nm particles possesses the same catalytic surface area as slurry particle reactor loaded at 30% w/w with 50 μm diameter particles.

The physical disparities between nanofluids and slurries suggest that their respective transport and reaction enhancement mechanisms are unrelated. In fact, early explanations for the observed nanofluid enhanced two-phase mass transport were drawn from the literature surrounding liquid emulsions instead of solid particle fluidized beds[65]. Unfortunately, concepts specific to gas absorption in aqueous oil emulsions [68], such as species shuttling, or grazing, and interfacial surface renewal have had limited success in fully explaining or predicting the mass transport rates observed in nanofluids.

Theoretical investigations on the use of nanofluids as a falling desiccant film by Ali, Vafai and Khaled in 2004 [71] also failed to predict the observations published this last year regarding nanofluid enhanced mass transport. Ali, Vafai and Khaled predicted a 30% increase in evaporative mass transport from nanofluids simply based on prior documented nanofluid enhanced thermal transport. In contrast, recent experiments performed under isothermal mass transport conditions, such as a nanofluid sparged reactor or bubble absorber, have exhibited anomalous improvement in mass transport between the liquid and gaseous phases [58, 65]. It is likely that both thermal and mass transport effects originate from a similar general mechanism, but there are a number of postulated secondary effects for nanofluid heat transfer that have no apparent analog in mass transport [64].

The observed enhanced thermal diffusion within stagnant nanofluids is a striking feature of the heat transfer field [72, 73], and our study has attempted to produce the mass

transport analog to that thermal phenomenon. Prior experiments claiming discovery of nanofluid enhanced species diffusion have been difficult to replicate [65, 74], and prompted our own careful analysis of the effect. Potential two-phase mass transport enhancement factors such as increased interfacial area for species absorption or stabilization of micro-bubbles have been explored by other authors [58], and shown incapable of facilitating the observed order of magnitude mass transport enhancement seen in nanofluids. Following the comparable heat transfer research, prior authors have also postulated a nano-enabled, improved Brownian diffusion mechanism to explain the nanofluid enhanced mass transport observations to some. Such a hypothesis however, has not yet been substantiated with reproducible experimental evidence to prove where and how the mechanism is enhancing two-phase mass transport.

To explain heat transfer enhancements observed in stagnant nanofluid films, previous publications have postulated a volumetric thermal conductivity enhancement owing to the Brownian motion of the nanoparticles themselves [57, 75]. The application of an alternative Brownian motion based boundary layer thinning mechanism has met with far less opposition than the former volumetric based hypothesis [60, 64]. Thermophoretic particle slip within the boundary layer has also been identified as a culpable agent for the nanofluid enhanced thermal transport [64], but it does not seem applicable to isothermal nanofluid enhanced mass transport. On the other hand, two-phase mass transport effects such as species shuttling at the interface due to chemical adsorption on nanoparticles or interfacial permeability enhancement due to nanoparticle-induced surface tension reduction are also curious explanations for the documented nanofluid mass transport behavior. The former has been examined in prior work [58], and

found to also be insufficient to wholly account for the enhanced mass transport observations. The latter has been explored for the first time in this current work by our comparison of variable nanofluid surface tension with two-phase mass transport enhancement.

# 7.0 Experiments in nanofluid enhanced mass transport

## 7.1 Diffusive transport

The ultimate role of particle diffusion within nanofluids is unclear; the size of their particulate constituents makes them subject to a wide variety of thermodynamic potentials and mechanical forces that may modify nanoparticle motion. The simplest, and often times dominant case of concentration gradient driven diffusion was isolated and tested in our study. Examination of this ubiquitous case reveals clues to the role played by Brownian motion of nanoparticles within generalized nanofluid transport physics. The effects were probed by measuring the binary diffusion coefficient of a dye within the nanofluid.

Despite the rich system information encoded within diffusivity measurements, the accurate acquisition of this data often requires considerable expertise in the art. Several experiments based on prior nanofluid and binary diffusion publications were evaluated for use in our work [74]. After repeating these experiments, and appraising their true utility, a classic Taylor-Aris dispersion [76, 77] experiment was decidedly the most robust and practical means of acquiring binary diffusion coefficient data.

As postulated by Taylor [76], and later extended in detail by Aris [77], the method is based upon several modifications of the two dimensional, convected radial diffusion equation for a tracer dye pulse injected into a laminar pipe flow

$$\frac{\partial^2 C}{\partial z^2}+\frac{1}{z}\frac{\partial C}{\partial z}+a^2\frac{\partial C^2}{\partial x^2}=\frac{a^2 U}{D}(1-2z^2)\frac{\partial C}{\partial x} \qquad (14)$$

where C is the concentration of an inert tracer dye (mol $L^{-1}$), a is the pipe radius (cm), U is the maximum flow velocity (cm $s^{-1}$), D is the binary diffusion coefficient for the dye within the flowing medium ($cm^2$ $s^{-1}$), z is a dimensionless radial coordinate (r $a^{-1}$), and x is the axial position (cm) along the conduit, measured from the point of injection. The problem is first simplified by assuming that axial convective transport dominates the axial diffusion of the solute. This condition is expressed as a diffusion Peclet number (Pe) whose value, according to Taylor, must be greater than 6.9

$$Pe=\frac{Ua}{D} \qquad (15)$$

Further simplifications can be made if the tracer concentration is measured once the hydrodynamic and diffusion profiles are fully developed. Due to transient radial mass transport, the diffusion profile develops as a blunt core, with trailing edges described by a higher order polynomial [76]. In contrast to radial transport, axial diffusion persists along the entire downstream channel length. Whereas the initial pulse injection is represented by a step-like concentration profile, axial diffusion increasingly broadens the peak at a rate that depends on the Peclet number and system geometry. According to Taylor's original analysis, the fully developed dye concentration profile is averaged over the channel cross section, which finally reduces equation (14) to

$$\frac{\partial C_m}{\partial t} = K \frac{\partial^2 C_m}{\partial x^2} \tag{16}$$

where $C_m$ is the profile averaged concentration, and K is the convected diffusion coefficient ($cm^2\ s^{-1}$)

$$K = \frac{a^2 U^2}{48D}. \tag{17}$$

Using Fourier transform techniques, or similarity analysis, a general solution to this initial value problem can be obtained

$$C_m(x,t) = \frac{1}{2\sqrt{\pi K t}} \int_{-\infty}^{\infty} f(\zeta) e^{\frac{-(x-\zeta)^2}{4Kt}} d\zeta \tag{18}$$

where $f(\zeta)$ are the initial dye concentration conditions everywhere along the tube after the dye is injected, and $\zeta$ (cm) is the axial position of the dye front. Applying the initial conditions of a discrete dye injection results in a traveling Gaussian pulse solution that continues to broaden as it moves down the channel. In our version of the experiment, the discrete dye injection is replaced by a continuous supply of dye laden fluid that can be modeled as a step change in dye concentration. The solution to equation (16) with the step change in boundary condition is a complimentary error function that broadens as the dye front travels down the channel. This experimental condition was found to produce the most practical and easily repeated experiment, thereby providing robust measurements of the binary diffusion coefficient for the dye in various media.

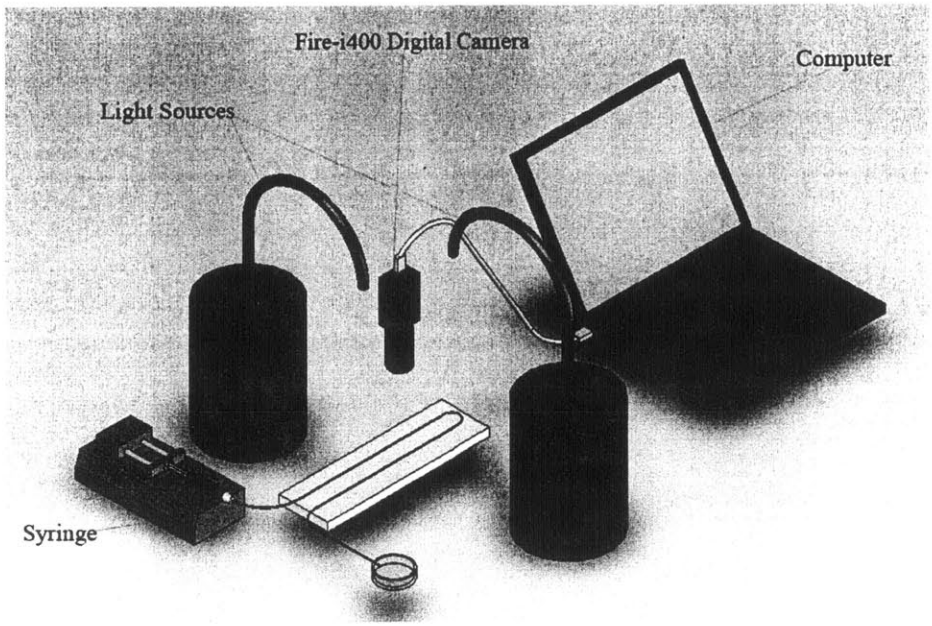


**Fig. 12 Taylor Dispersion Experiment**

The test section was prepared by fixing a tube with an inner diameter of 0.0254 cm to a rigid plate. To prepare each experiment, the tube was filled with the non-dyed sample fluid, and then connected to a Harvard PHD 4400 syringe pump which injected the dyed test fluid at a nominal rate of 1mL/hr. Special care was taken to prevent the introduction of air bubbles into the tube. Moreover, the test samples were all maintained at 22 C prior to experimentation, and two Fiber-Lite Model 190 fiber optic lamps were used to illuminate the test section from opposite sides of the tube, providing a bright viewing area without significant radiant heating.

Situated 116 cm down the tube from the syringe, a Unibrain Fire-i400 color camera was set to take pictures every 10 seconds, for a total of 125 frames. This position allowed sufficient time for the flow to become fully developed, and for the concentration profile to broaden sufficiently for a precise optical measurement of the dye concentration.

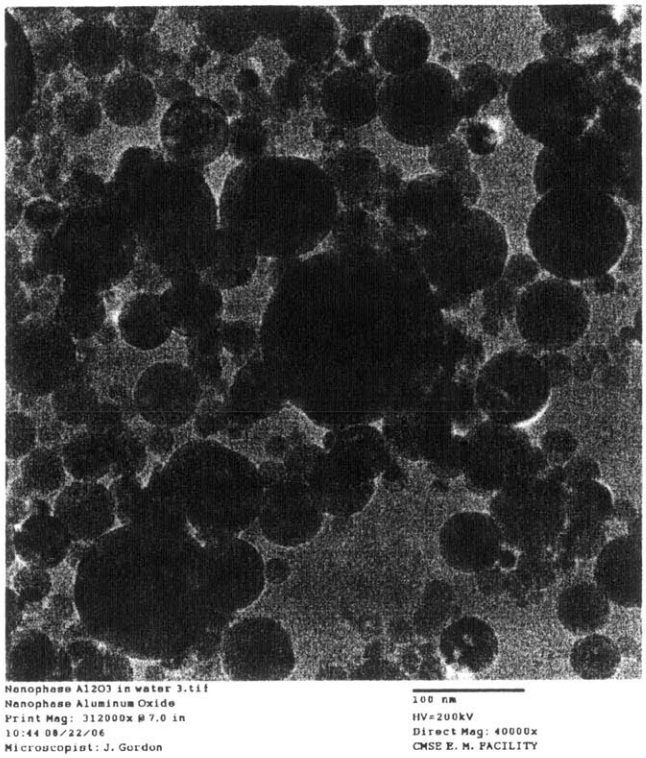


**Fig. 13 TEM of Aluminum Oxide Nanoparticle**

The dye solution was prepared by taking a 3mL sample of the test fluid and mixing it with several drops of commercially available Allura Red stock solution. In addition to DI water, an Aluminum Oxide nanofluid and solutions of F-60 Pluronics and Sodium Dodecyl Sulfate (SDS) were tested for anomalous binary diffusion effects. The aluminum oxide (50 nm average diameter, poly-disperse) nanoparticles were procured from Nanophase Inc., at a stock concentration of 0.27 % w/w, without any surfactant. Stock solution samples were drawn into fresh glass beakers and diluted with DI water to .5%, .7% and 1% w/w suspensions for testing. The SDS (roughly 2nm diameter micelles) was purchased from Sigma-Aldrich, and dissolved in DI water at 0.5 mM, 5 mM and 10 mM concentrations, to probe the diffusion effects above and below the measured critical micellar concentration (CMC) of 3mM. The F-60 Pluronics were also acquired from

Sigma-Aldrich and tested at 2% and 5% w/w in DI water, to probe the effects of a non-ionic, tri-block polymer chain surfactant. To ensure stable dispersion of the suspensions, each test sample was sonicated for two hours prior to experimentation. The samples were also re-sonicated prior to experimentation if they sat stagnant for more than 1 hour between experiments. Each test was repeated in triplicate, with appropriate equipment cleaning and resetting between trials. Figures 12 and 14 indicate the method of data acquisition performed in this diffusion experiment.

An image collection system was employed to capture the channel color every ten seconds from the start of fluid injection. Figure 12 illustrates the camera setup, which employed a Unibrain Fire-i400 color camera in series with a Navitar 7000 tv zoom lense, at 6X magnification and a numerical aperture of 0.0179. The images taken measured 640 x 480 pixels, and correspondingly had 256 pixels per mm. The camera was set to a gain of 1 and the axial variation of channel diameter due to blur was found to be +/- 3 pixels. Images (a), (b), and (c) in figure 14 show the changing channel color as the experiment is executed, along with the representative pixilation data collection locations. The corresponding graph in image (d) is the red pixel value of the channel, averaged amongst the five locations where the measurement is taken, versus time from injection. The raw data typically starts at a red value of 230, indicative of zero concentration or white background, and saturates at 150 once the dye front has traveled sufficiently downstream.

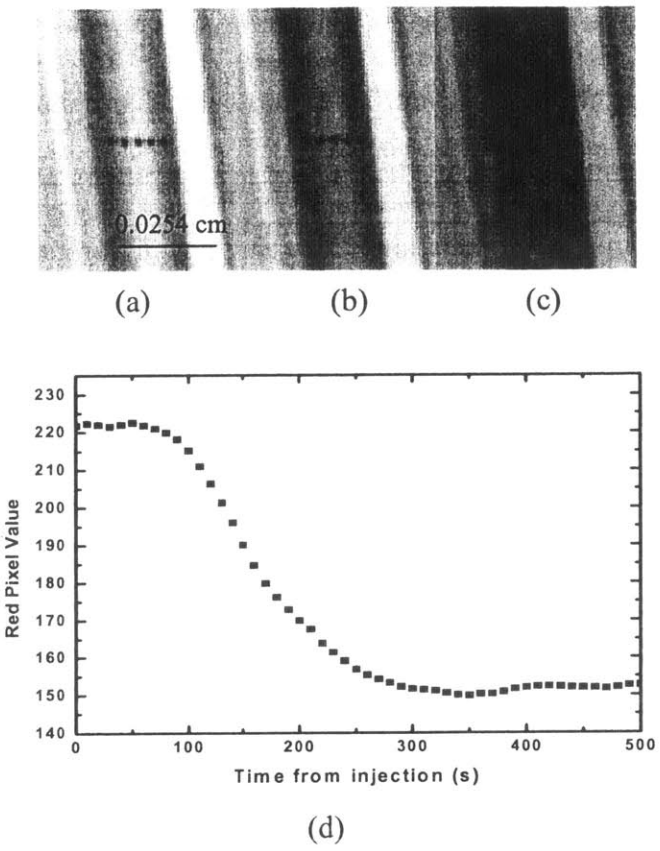


**Fig. 14 (a) the channel before the dye (b) the channel during passage of the front (c) fully saturated channel (d) graph of red pixel value vs. time, averaged from five pixels across the channel**

To ensure an accurate representation of the front, each graph is constructed from the averaged raw pixilation data collected at five, horizontal, collinear pixels anchored at the center of the channel, as shown in figures 14 (a)-(c). Moreover, eight different locations of five pixels along the imaged channel length were analyzed in this same fashion for each experiment. Having performed each experiment in triplicate, with at least 125 frames per experiment, and eight different measurement locations comprised of five pixels, each of our final calculations was based on the analysis of 15,000 data points.

A Matlab script was written to collect and evaluate the images. Ultimately, the information was fit with a complimentary error function according to the solution of equation (16), whose width was used to calculate the binary diffusion coefficient via

equation (17). In addition to the averaged data, the script quantified the error propagation from each step of the analysis.

To reduce computation time, the raw data was pre-processed by a Savitsky-Golay (SG) filter that preserved any significant high frequency data, as well as the higher moments of the major peak data. The SG filter is a common feature of the Matlab filter toolbox and consists of fitting small data spans with polynomials of any order greater than three. In this case the span was five and the polynomial order nineteen. The higher order and smaller span were chosen specifically to eliminate high amplitude, high frequency noise that originated from variations in lighting and reflected color intensity. After filtering, the data was normalized according to the initial and final dye concentration and then fit with a complimentary error function via a robust weighting algorithm that was resistant to outliers. The algorithm was based on a small-span least squares regression that weighted data proportionally to its distance from an initial mean value estimate, and altogether eliminated single point outlying variations beyond 30%.

Eight measurement locations were chosen for each of the three trials of each experiment. The cumulative measurements from 24 individual data sets were used to construct a final error function fit to deduce the binary diffusion coefficient of the dye for each experimental fluid. The size of the data sets also provided sufficient volume to accurately calculate the errors attributed to measurement and analysis. In contrast to the Taylor dispersion experiment, the oxygenation rate data acquisition did not require an elaborate data collection and filtering protocol. This simplification is attributed to our use of a commercial dissolved oxygen meter and associated acquisition and analysis module that output both raw and normalized data to a computer.

## 7.2 Bulk two-phase mass tansport

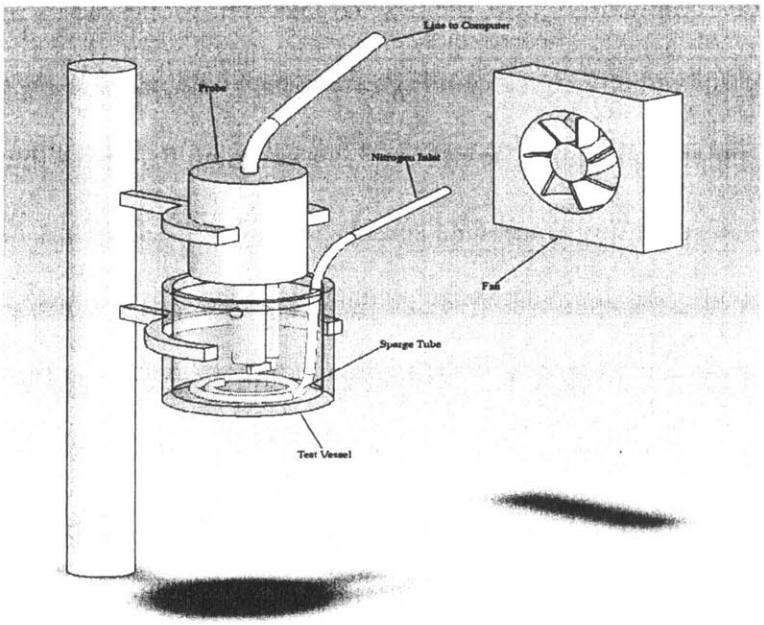


**Fig. 15 Oxygenation Experiment Apparatus**

A YSI 5010 BOD Clarkson electrode type oxygen probe, with YSI 5100 associated data acquisition module was used to measure the oxygen concentration within a well stirred 200 ml sample of fluid. The acquisition module was connected to a computer via an RS-232 cable, where the data was continuously recorded for the duration of the experiment. The probe was equipped with a stirrer to circulate the liquid and refresh the oxygen content at the probe surface. In addition, the probe housed a thermocouple and pressure sensor to record temperature and barometric pressure, which were immersed in the sample during the experiment. The probe was calibrated in air, and pure nitrogen before each use, and the probe tip was replaced after every three experiments. A DI water control experiment was performed every five days during the data collection period to establish a robust baseline.

A sparging tube was immersed in the sample vessel along with the probe, which delivered pure nitrogen gas used for the de-oxygenation of the sample. Nitrogen was exhausted through the sample until the probe measured zero oxygen concentration, at which point the data recorder was initiated and the nitrogen tank shut off. At the same time, the probe was given a light tap to dislodge any nitrogen bubbles caught on the probe surface. The nitrogen exhaust rate was also controlled to prevent surface frothing.

Each experiment was run for approximately 20 minutes, which provided adequate time for the sample to re-attain dissolved oxygen saturation. As with the Taylor dispersion work, these experiments were performed in triplicate for each fluid sample. In addition to the samples and quantities tested in the diffusion experiments, suspensions each of a novel ferrofluid-carbon nanotube (FFCNT) composite and cetyl-trimethyl ammonium bromide (CTAB) were also tested.

The FFCNT composites (with 50 nm diameter by 7 $\mu$m in length) were created according to our prior work [78], and included here to probe geometric factors that may play a role in nanofluid transport. The FFCNT particles were stabilized against sedimentation by the addition of CTAB to the suspension, resulting in a 5 mM CTAB solution. To isolate the performance of the FFCNT, the data from the suspension was carefully compared against a control 5 mM solution of CTAB. The CTAB was also acquired from Sigma-Aldrich and tested as an additional micelle forming surfactant, albeit with cationic surface charge as oppose to the anionic charge on the SDS. Like SDS, CTAB forms micelles approximately 2 nm in a diameter, but with a measured CMC of 0.3 mM. The CTAB was not tested in the Taylor-Aris experiment due to the potential for spontaneous electrostatic agglomeration between CTAB and Allura dye.

As shown in figure 15, a fan was also used to test the gas side transport resistance. The fan (1.44 W DC) was positioned at a slight angle to the sample beaker, and was used to increase air circulation without generating swells on the liquid surface. Experiments were repeated with and without the fan in order to generate a data shift that would indicate the influence of the variable air circulation and hence the relevance of the gaseous transport resistance to overall nanofluid enhanced two-phase mass transport.

The normalized output data from the YSI 5100 module was fit with an exponential decay function to determine the oxygen infiltration time constant for the fluid. This analytical fit is commensurate with a standard lumped capacitance model for this experiment, which is detailed in Olle et al [58]. Again following that same work, we defined and evaluated the mass transport enhancement of a nanofluid as the ratio between the DI water and nanofluid infiltration time constants.

$$E \equiv \frac{\tau_{DI}}{\tau_{nanofluid}} \tag{19}$$

Before making any oxygenation measurements, a Kruss K10ST digital tensiometer with platinum plate geometry was used to measure the surface tension of each sample.

## 8.3 Interfacial transport

The sample surface tension was used as a metric for the gas-liquid interfacial adsorption of a gaseous solute. For a Gibb's adsorption isotherm, the surface tension and gaseous solute interface adsorption at a quiescent liquid surface are related by

$$\Gamma = -\frac{1}{2.3RT}\frac{d\gamma}{d(\log\alpha)} \tag{20}$$

where $\gamma$ (mN $m^{-1}$) is the surface tension, $\Gamma$ (mol $m^{-2}$) is the surface adsorption,

R (J $mol^{-1}$ $K^{-1}$) is the universal gas constant, T (K) is the temperature, and $\alpha$ is the thermal activity of the surface. In general, pure surface adsorption increases with decreasing surface energy, and hence decreasing surface tension. On the other hand, the solvation rate of gas molecules can also be increased by the formation of stable micro-bubbles at the interface. Such transport vesicles help to shuttle solute into the solvent faster than pure adsorption. As micro-bubbles are also strongly surface tension dependent, surface tension may in fact play a number of roles in controlling the dissolution of oxygen in the sparged reactor experiments. At the same time, while the addition of surfactants to a solution will reduce surface tension, they also inhibit interfacial transport by adding a monolayer surface coating. Clearly there are multiple avenues by which surface tension can influence two-phase mass transport, and a per sample direct comparison between the surface tension and oxygenation rate data of each nanofluid is not sufficient to explain the interaction. On the other hand, a simple correlation between the two measurable quantities can form the foundation for future investigations into the precise relationship between surface tension and oxygenation rate in nanofluids.

# 8.0 Results of nanofluid mass transport experimentation

## 8.1 Taylor-Aris diffusion data

The measurement of binary diffusion coefficients via the Taylor dispersion experiment yielded no significant differences between nanofluids and DI water.

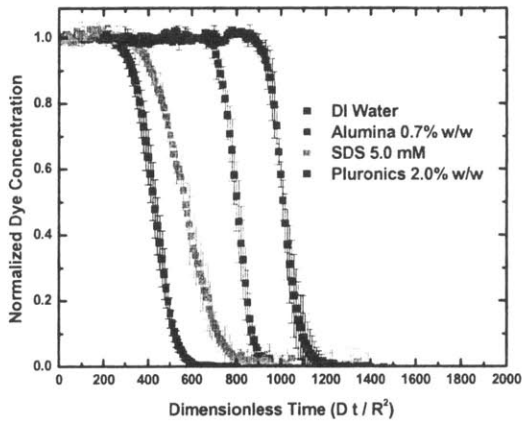


**Fig. 16 Comparison of dye profile for DI water, alumina nanofluid, SDS solution, and pluronics**

Figure 16 presents a direct comparison of DI water to a representative concentration from each of the three families of experimental liquids. The time shifts between the spectra are arbitrary, and were introduced to simplify the presentation of the critical data. Each set was normalized on the y-axis according to the initial dye concentration for each experiment. The experimental time was also normalized by the channel radius and the binary diffusion coefficient calculated from each experiment. Allura dye, in water was found to have a binary diffusion coefficient of $4.2 \times 10^{-6}$ $cm^2$ $s^{-1}$. At all tested concentrations, the SDS, Pluronic and Alumina experimental liquids produced the same binary diffusion coefficient within 50%, with an average error for all measurements of 20% or less. The manufacturer's quoted binary diffusion coefficient is roughly $10^{-6}$ $cm^2$ $s^{-1}$, which is in satisfactory agreement with our more accurate measurements.

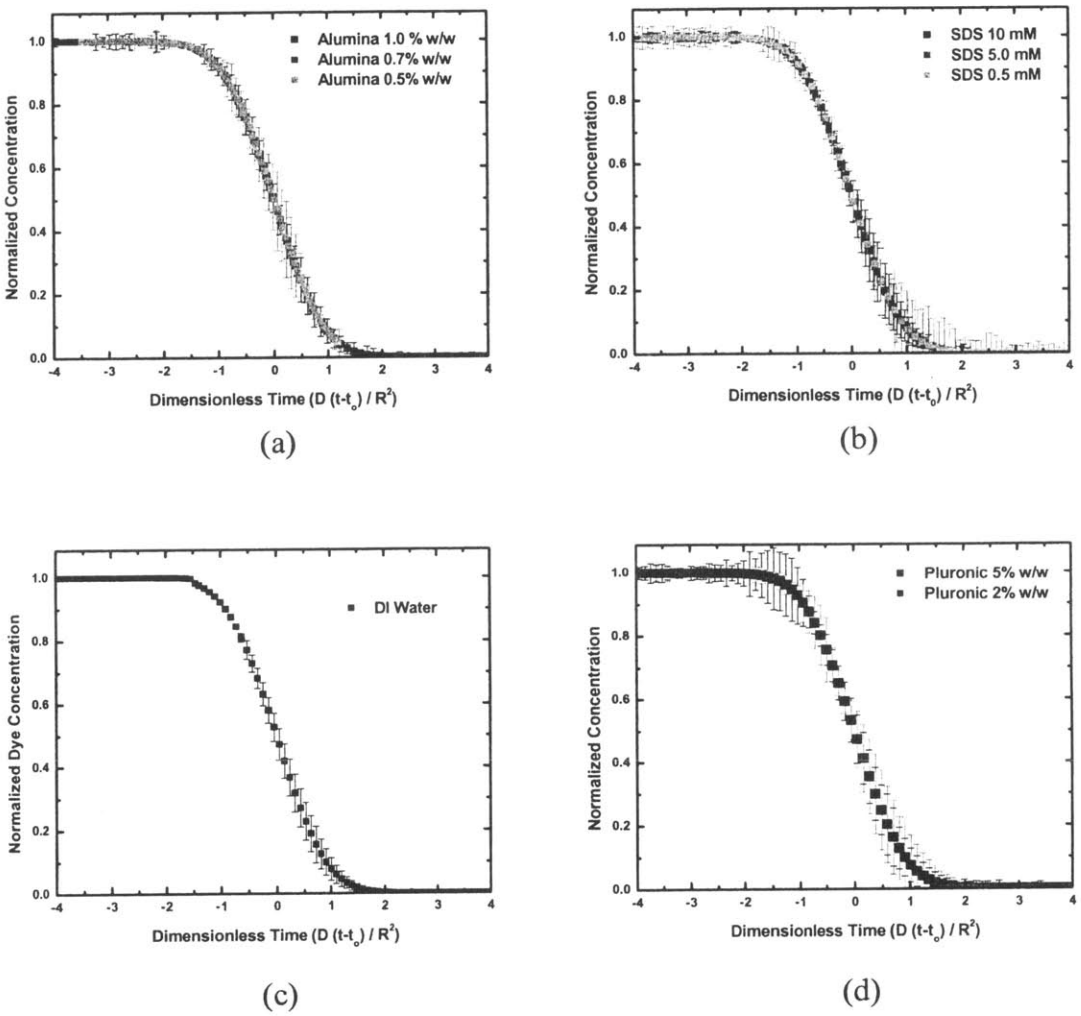


**Fig. 17 (a) alumina (b) SDS and (c) DI Water and (d) Pluronic dye profiles at various concentrations**

Figure 17 (a)-(d) compare the data for DI water with different concentrations of each family of experimental liquids. These profiles have been normalized as before, with the addition of a time shift that overlays each set within the same family. The errorbars on the normalized scale in figures 16 and 17 represent the percentage difference between the maximum or minimum measured value of that data point with respect to its plotted average value. In contrast to the data found in the Taylor-Aris experiments, oxygenation rate enhancements as great as 400% were observed for several different nanofluids.

## 8.2 Oxygenation rate data

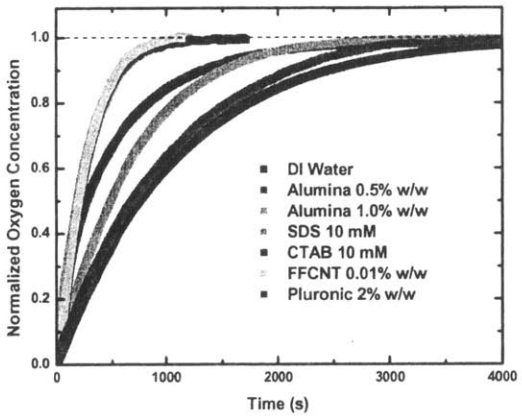


**Fig. 18 Oxygenation rate for several nanofluids versus DI water**

The oxygen infiltration time constants for the FFCNT composite, 10 mM CTAB and 10 mM SDS were all found to be approximately 260 s +/- 4%. With water having a time constant of 1067 s, these three nanofluids exhibit a four fold enhancement in oxygenation rate. A saturation effect is also evident in figure 18, where 0.5% w/w alumina shows a two fold enhancement, but 1.0% w/w alumina only shows a factor of five-thirds. The micellar nanofluid systems also exhibited saturation phenomenon.

Unlike the alumina however, the micellar suspensions exhibited saturation at an upper critical concentration as well as a total loss of enhancement at concentrations below the CMC.

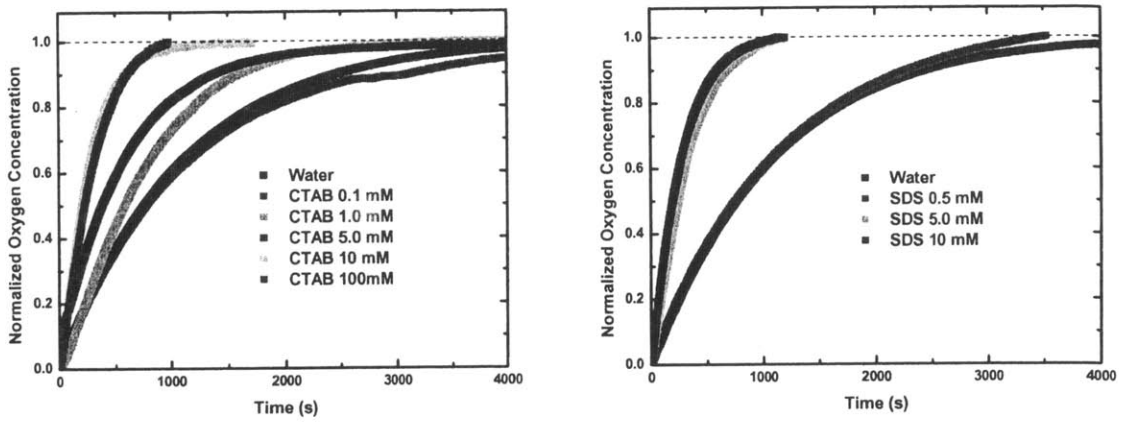


(a) (b)

**Fig. 19 (a) CTAB and (b) SDS oxygenation behavior**

The lowest tested CTAB and SDS concentrations were below their CMC, and the resulting loss of enhancement at those levels is shown as a red line in each figure. The SDS further shows a rapid saturation trend as the concentration approaches 10 mM, with an approximate saturation enhancement of four. The CTAB shows a similar saturation trend, with a critical concentration near 10 mM, albeit with a slower approach to the same saturation enhancement factor. The repetition of each of these oxygenation experiments with an air circulating fan did not produce any shift of the data.

## 8.3 Surface tension results

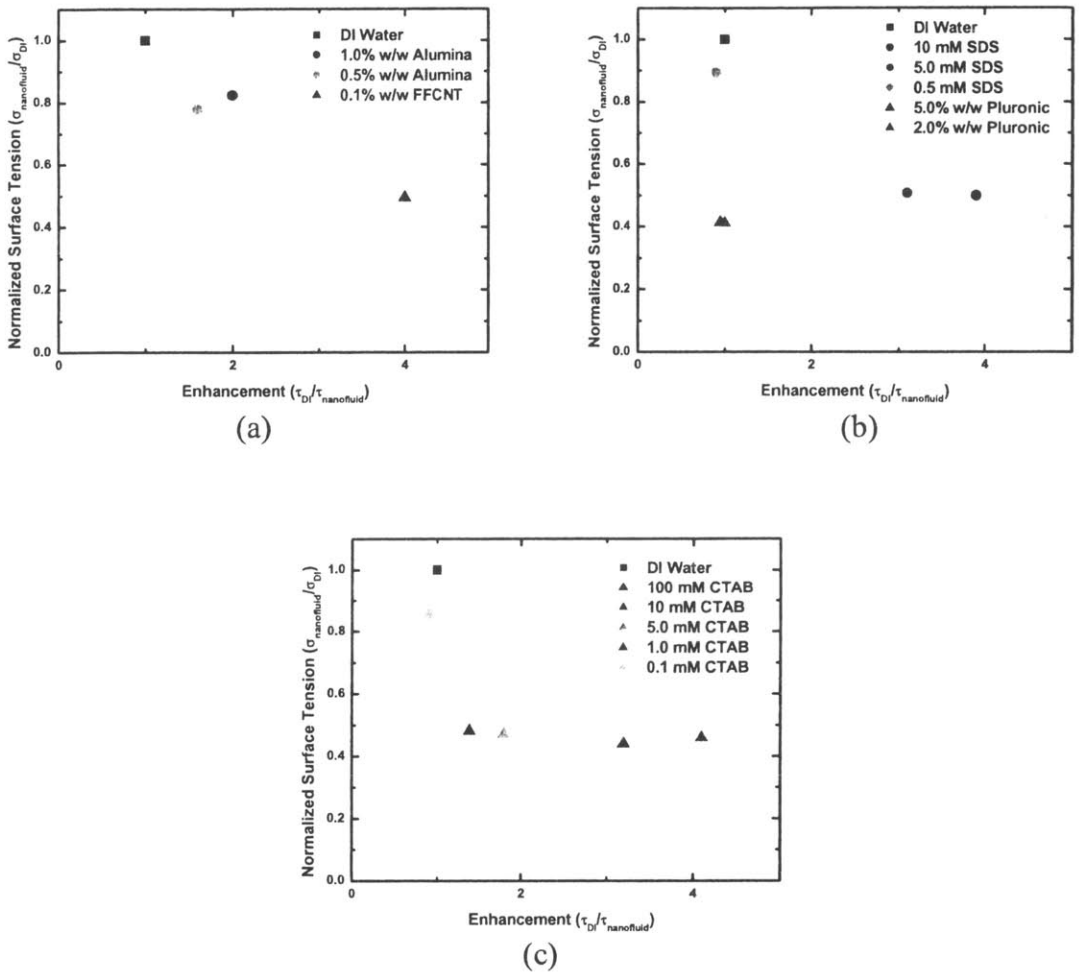


**Fig. 20 Comparison of Surface Tension reduction and Transport Enhancement within (a) Alumina and DI water, (b) SDS, Pluronics, and DI Water, (c) CTAB and DI Water**

Figure 20 (a)-(c) compares nanofluid surface tension data, normalized by the value for DI water, with the enhancement measurements drawn from the oxygenation experiments. Across all three figures it is clear that a larger surface tension reduction in the nanofluid does not imply a greater oxygenation rate enhancement factor. The Pluronic, SDS, and CTAB systems at sufficient concentrations all result in reducing the nominal water surface tension from 72.8 mN m to roughly 34 mN m. Only the SDS and

CTAB nanofluids, however, also produce a significant enhancement with that surface tension reduction. Furthermore, Pluronics at a reduced surface tension of 33 mN m, as well as sub-CMC CTAB and SDS solutions at nearly the surface tension of pure water, all result in a 15% decrease in oxygenation rate below that of pure water.

## 9.0 Model for nanofluid mass transport

Within the limitations of the Taylor-Aris experiment, nanofluids did not show any Brownian diffusion based mass transport enhancement. Given the error propagation through the analysis of the diffusion data, the nanofluid diffusion coefficient could exceed that of water by a maximum of 70%. At a water based binary diffusion coefficient of $4 \times 10^{-6}$ $cm^2$ $s^{-1}$, the maximum observed nanofluid diffusion coefficient was roughly $7 \times 10^{-6}$ $cm^2$ $s^{-1}$. Conversely, other measurements also showed the dye diffusivity in water to exceed that in nanofluids by as much as 50%. Considering the acceptable inaccuracies of diffusion data, the overlapping measurement errors between each data set, and the data volume for each experiment, the evidence strongly suggests that nanofluids do not exhibit any novel diffusion properties.

In stark contrast, the bulk oxygenation measurements clearly show significant mass transport enhancements within several nanofluid samples. These results corroborate previously published data, and also extend the field to include micellar nanofluids. The saturation effects seen in 1% w/w alumina, 10 mM SDS, and 10 mM CTAB have also been observed elsewhere with 1% w/w magnetite nanoparticles. What has previously not been shown, however, is the enhancement phenomenon within

micellar suspensions and the elimination of that effect at surfactant concentrations below the CMC.

Whereas CTAB and SDS micelles are known to be media wherein oxygen is more soluble than in water, their increased solubility is insufficient to enhance mass transport rates via a vesicle transport mechanism. The enhancement trends witnessed within alumina, FFCNT composite, SDS and CTAB suggest that the critical component for this effect is the existence of a nanostructure with a dimension less than 50 nm.

The loss of enhancement when the CTAB or SDS micelles degenerate to a monolayer coating at sub-CMC concentrations is strong evidence that any small diameter nanoparticle suspension can exhibit enhanced mass transport. Other studies have also shown that beyond the 1% w/w concentration, nanoparticles tend to agglomerate into larger particles. The alumina transport saturation effect observed at this same concentration may therefore be due to the formation of larger alumina agglomerates that surpass the suspected size limit for enhancement. Conversely, CTAB and SDS micelles do not approach the 50 nm size limit as their solution concentration is increased. Therefore, the observed CTAB and SDS saturation suggests that the enhancement may be limited by a critical particle number density as well as a critical nanoparticle size.

Figures 18-19 show the FFCNT suspension transport rate to exceed the performance of the 5mM CTAB control experiment by a factor of 1.25, indicating that the CTAB added to the suspension for sedimentation stability was not solely responsible for the FFCNT measurement. The FFCNT dimensions are 50 nm diameter by 7 $\mu$m in length, and hence its response further supports the hypothesis that mass transport enhancement requires some critical dimension at roughly 50 nm or below.

Surface tension measurements combined with the oxygenation data prove the absence of a significant interfacial transport resistance. In fact, the Pluronic and sub-CMC CTAB and SDS solutions show a reduction in transport rate to below that seen in water. At those particular tested concentrations, this response is expected due to the formation of a surfactant monolayer at the interface. CTAB and SDS also seem to exhibit a trend of increasing enhancement factor with decreasing surface tension. This is likely an artifact from the increasing surfactant concentration that also acts to reduce surface tension. Coincidentally, the oxygenation data for CTAB and SDS in figures 19 (a) and (b) also show a trend for increasing enhancement with increasing surfactant concentration. Finally, figure 20 also indicates that the alumina oxygenation rate enhancement occurs with only a minor reduction of the interfacial tension. In addition to the data that show a negligible interfacial transport resistance, the lack of any oxygenation rate data shift with the addition of an air circulator also indicates that the gas side transport resistance is insignificant.

# 10.0 Conclusions

## 10.1 Magnetic carbon nanotubes

We have reviewed the extensive formulation techniques that exist to create magnetically modified carbon nanotubes and their suitability for a wide variety of applications. Chemical and physical techniques have been proven to introduce a diverse range of magnetic materials within CNTs, thus dramatically enhancing our ability to manipulate individual nanotubes, functionalize their surface, and induce self-assembly of complex nanostructures. Several of these techniques have been utilized to create novel

MR fluids, and their viscometric properties have been demonstrated to enrich the range of rheological behavior that can be achieved with this class of non-Newtonian fluids. With the successful coupling of magnetic character to CNTs, it is possible to explore other interesting combinations of magnetism with unique CNT properties such as high electrical and thermal conductivity. Ongoing work includes combined magneto-electric rheology, which capitalizes on the strong dielectrophoretic forces generated within the highly electrically conducting CNT, and the magnetic coating surrounding the CNT.

## 10.2 Nanofluid mass transport

The combined lack of any observed volumetric Brownian diffusion enhancement, negligible interfacial and gas side transport resistances, minor surface area augmentation effects, and plausible vesicle based enhanced transport mechanism, suggests that the underpinnings of nanofluid enhanced multi-phase mass transport lies within the mechanics of a thin liquid layer directly beneath the gas-liquid interface. Additionally, this mechanism must at least depend on both the average particle size and number density.

This work has also shown that nanofluid phenomenon can be observed in any system containing particles with a dimension below 50 nm, including polymer micelles and carbon nanotubes. Further research in multi-phase transport should be performed under conditions where the gas and liquid dynamics are well characterized and controlled. Such an extension could be used to probe the exact role of nanoparticles within the mechanics of the liquid boundary layer, and hence their influence on the mass transfer resistance of the liquid.

Finally, the success of the oxygenation rate studies support the aforementioned applications of nanofluids as a potential commercial alternative to fluidized beds and other multi-phase heat and mass exchanger systems. The relative low costs of micellar nanoparticles also offer a practical alternative to nanofluids based off more exotic and expensive nanoparticles that show the same performance characteristics.

**Nomenclature**

$V_o$ – sedimentation velocity (m/s)
$\varepsilon$ - magnetic shell thickness (m)
$L$ – aggregate length (m)
$\rho_s$ - particle density (kg/m$^3$)
$\rho_f$ - fluid density (kg/m$^3$)
$g$ – gravitational acceleration (9.81 m/s$^2$)
$a$ – particle, tube radius (m)
$\eta$ - fluid viscosity (Pa s)
$\mu_o$ – permeability of free space ($4\pi \times 10^{-7}$ N/A$^2$)
$H$ – magnetic field (A/m)
$\chi$ - magnetic susceptibility
$\lambda$ - ratio of magnetic aggregation force versus Brownian dispersion force
$k_B$ – Boltzmann constant ($1.38 \times 10^{-23}$ J/K)
$T$ – temperature (K)
$Ma$ – Mason number, dimensionless ratio of hydrodynamic to magnetic forces
$\sigma_c$ – critical yield stress (Pa)
$\sigma$ - applied shear stress (Pa)
$\phi$ - particle volume fraction (v/v)
$G$ – elastic modulus (Pa)
$C$ – *concentration (mol L$^{-1}$)*
$a$ – *channel radius (cm)*
$U$ – *maximum flow velocity (cm s$^{-1}$)*
$D$ – *binary diffusion coefficient (cm$^2$ s$^{-1}$)*
$z$ – *dimensionless radial coordinate*
$x$ – *axial position along channel (cm)*
$C_m$ – *cross sectional averaged dye concentration (mol L$^{-1}$)*
$Pe$ – *diffusion Peclet number*
$K$ – *convected diffusion coefficient (cm$^2$ s$^{-1}$)*
$\zeta$ – *axial position of dye front (cm)*
$E$ – *oxygenation rate enhancement factor*
$\tau_{DI}$ – *DI water oxygen infiltration time constant (s)*
$\tau_{nanofluid}$ – *nanofluid oxygen infiltration time constant (s)*
$\Gamma$ – *surface adsorption (mol m$^{-2}$)*

$\gamma$ – *surface tension (dynes cm$^{-1}$)*
*R – universal gas constant (J mol$^{-1}$ K$^{-1}$)*
*T – temperature (K)*
$\alpha$ – *surface thermal activity*

**References**


[1]. Dresselhaus, M.S., Dresselhaus, G., and Jorio, A., 2004, "Unusual properties and structure of carbon nanotubes", Annual Review of Materials Research. **34**: p. 247-278.

[2]. Feynman, R., *There is plenty of room at the bottom.* 1969.

[3]. Rosensweig, R.E., *Ferrohydrodynamics.* 1985, New York: Dover.

[4]. Ajayan, P.M., Ebbesen, T.W., Ichihashi, T., Iijima, S., Tanigaki, K., and Hiura, H., 1993, "Opening Carbon Nanotubes with Oxygen and Implications for Filling", Nature. **362**(6420): p. 522-525.

[5]. Ajayan, P.M. and Iijima, S., 1993, "Capillarity-Induced Filling of Carbon Nanotubes", Nature. **361**(6410): p. 333-334.

[6]. Bao, J.C., Tie, C., Xu, Z., Suo, Z.Y., Zhou, Q.F., and Hong, J.M., 2002, "A facile method for creating an array of metal-filled carbon nanotubes", Advanced Materials. **14**(20): p. 1483

[7]. Leonhardt, A., Ritschel, A., Kozhuharova, R., Graff, A., Muhl, T., Huhle, R., Monch, I., Elefant, D., and Schneider, C.M., 2003, "Synthesis and properties of filled carbon nanotubes", Diamond and Related Materials. **12**(3-7): p. 790-793.

[8]. Korneva, G., Ye, H.H., Gogotsi, Y., Halverson, D., Friedman, G., Bradley, J.C., and Kornev, K.G., 2005, "Carbon nanotubes loaded with magnetic particles", Nano Letters. **5**(5): p. 879-884.

[9]. Wu, H.Q., Wei, X.W., Shao, M.W., Gu, J.S., and Qu, M.Z., 2002, "Preparation of Fe-Ni alloy nanoparticles inside carbon nanotubes via wet chemistry", Journal of Materials Chemistry. **12**(6): p. 1919-1921.

[10]. Muhl, T., Elefant, D., Graff, A., Kozhuharova, R., Leonhardt, A., Monch, I., Ritschel, M., Simon, P., Groudeva-Zotova, S., and Schneider, C.M., 2003, "Magnetic properties of aligned Fe-filled carbon nanotubes", Journal of Applied Physics. **93**(10): p. 7894-7896.

[11]. Zhenyu Sun, Z.L., Yong Wang, J. Bursik, M. Kadlecikov, 2005, "Fabrication and characterization of magnetic carbon nanotube composites", Journals of Materials Chemistry. **15**(42): p. 4497-4501.

[12]. Lafdi, K., Chin, A., Ali, N., and Despres, J.F., 1996, "Cobalt-doped carbon nanotubes: Preparation, texture, and magnetic properties", Journal of Applied Physics. **79**(8): p. 6007-6009.

[13]. Rao, C.N.R., Sen, R., Satishkumar, B.C., and Govindaraj, A., 1998, "Large aligned-nanotube bundles from ferrocene pyrolysis", Chemical Communications(15): p. 1525-1526.

[14]. Liu, S.W., Tang, X.H., Mastai, Y., Felner, I., and Gedanken, A., 2000, "Preparation and characterization of iron-encapsulating carbon nanotubes and nanoparticles", Journal of Materials Chemistry. **10**(11): p. 2502-2506.

[15]. Liu, S.W., Zhu, J.J., Mastai, Y., Felner, I., and Gedanken, A., 2000, "Preparation and characteristics of carbon nanotubes filled with cobalt", Chemistry of Materials. **12**(8): p. 2205-2211.

[16]. Banhart, F., Grobert, N., Terrones, M., Charlier, J.C., and Ajayan, P.M., 2001, "Metal atoms in carbon nanotubes and related nanoparticles", International Journal of Modern Physics B. **15**(31): p. 4037-4069.

[17]. Zhang, X.X., Wen, G.H., Huang, S.M., Dai, L.M., Gao, R.P., and Wang, Z.L., 2001, "Magnetic properties of Fe nanoparticles trapped at the tips of the aligned carbon nanotubes", Journal of Magnetism and Magnetic Materials. **231**(1): p. L9-L12.

[18]. Georgakilas, V., Tzitzios, V., Gournis, D., and Petridis, D., 2005, "Attachment of magnetic nanoparticles on carbon nanotubes and their soluble derivatives", Chemistry of Materials. **17**(7): p. 1613-1617.

[19]. Peng, D.L., Zhao, X., Inoue, S., Ando, Y., and Sumiyama, K., 2005, "Magnetic properties of Fe clusters adhering to single-wall carbon nanotubes", Journal of Magnetism and Magnetic Materials. **292**: p. 143-149.

[20]. Stoffelbach, F., Aqil, A., Jerome, C., Jerome, R., and Detrembleur, C., 2005, "An easy and economically viable route for the decoration of carbon nanotubes by magnetite nanoparticles, and their orientation in a magnetic field", Chemical Communications(36): p. 4532-4533.

[21]. Choi, Y.C., Shin, Y.M., Lee, Y.H., Lee, B.S., Park, G.S., Choi, W.B., Lee, N.S., and Kim, J.M., 2000, "Controlling the diameter, growth rate, and density of vertically aligned carbon nanotubes synthesized by microwave plasma-enhanced chemical vapor deposition", Applied Physics Letters. **76**(17): p. 2367-2369.

[22]. Bottini, M., Tautz, L., Huynh, H., Monosov, E., Bottini, N., Dawson, M.I., Bellucci, S., and Mustelin, T., 2005, "Covalent decoration of multi-walled carbon nanotubes with silica nanoparticles", Chemical Communications(6): p. 758-760.

[23]. Liu, J., Rinzler, A.G., Dai, H.J., Hafner, J.H., Bradley, R.K., Boul, P.J., Lu, A., Iverson, T., Shelimov, K., Huffman, C.B., Rodriguez-Macias, F., Shon, Y.S., Lee, T.R., Colbert, D.T., and Smalley, R.E., 1998, "Fullerene pipes", Science. **280**(5367): p. 1253-1256.

[24]. Cao, H.Q., Zhu, M.F., and Li, Y.G., 2006, "Decoration of carbon nanotubes with iron oxide", Journal of Solid State Chemistry. **179**(4): p. 1208-1213.

[25]. Wu, H.Q., Cao, Y.J., Yuan, P.S., Xu, H.Y., and Wei, X.W., 2005, "Controlled synthesis, structure and magnetic properties of Fe1-xNix alloy nanoparticles attached on carbon nanotubes", Chemical Physics Letters. **406**(1-3): p. 148-153.

[26]. Li, Y.G.a.D., 1999, "The van der Waals Interaction between a Spherical Particle and Cylinder", Journal of Colloid and Interface Science. **217**(1): p. 60-69.

[27]. Kirsch, V.A., 2003, "Calculation of the van der Waals force between a spherical particle and an infinite cyinder", Advances in Colloid and Interface Science. **104**: p. 311-324.

[28]. Correa-Duarte, M.A., Grzelczak, M., Salgueirino-Maceira, V., Giersig, M., Liz-Marzan, L.M., Farle, M., Sierazdki, K., and Diaz, R., 2005, "Alignment of carbon nanotubes under low magnetic fields through attachment of magnetic nanoparticles", Journal of Physical Chemistry B. **109**(41): p. 19060-19063.

[29]. Pu, H.T. and Jiang, F.J., 2005, "Towards high sedimentation stability: magnetorheological fluids based on CNT/Fe3O4 nanocomposites", Nanotechnology. **16**(9): p. 1486-1489.
[30]. Razavian S M, W.R.B., Fisher T C and Meiselman H J, 1997, Biorheology. **34**: p. 349-362.
[31]. Klingenberg, D.J., 2001, "Magnetorheology: Applications and challenges", Aiche Journal. **47**(2): p. 246-249.
[32]. Stanway, R., 2004, "Smart fluids: current and future developments", Materials Science and Technology. **20**(8): p. 931-939.
[33]. Bossis, G., Lacis, S., Meunier, A., and Volkova, O., 2002, "Magnetorheological fluids", Journal of Magnetism and Magnetic Materials. **252**(1-3): p. 224-228.
[34]. Ginder, J.M., Davis, L.C., and Elie, L.D., 1996, "Rheology of magnetorheological fluids: Models and measurements", International Journal of Modern Physics B. **10**(23-24): p. 3293-3303.
[35]. Tao, R., 2001, "Super-strong magnetorheological fluids", Journal of Physics-Condensed Matter. **13**(50): p. R979-R999.
[36]. Larson, R.G., *The Structure and Rheology of Complex Fluids*. 1999, New York: Oxford University Press.
[37]. Rabinow, J., 1948, AIEE Trans. **67**: p. 1308.
[38]. Winslow, *2,417,850*. 1947: US.
[39]. Wen, W.J., Huang, X.X., Yang, S.H., Lu, K.Q., and Sheng, P., 2003, "The giant electrorheological effect in suspensions of nanoparticles", Nature Materials. **2**(11): p. 727-730.
[40]. Promislow, J.H.E., Gast, A.P., and Fermigier, M., 1995, "Aggregation kinetics of paramagnetic colloidal particles", The Journal of Chemical Physics. **102**(13): p. 5492-5498.
[41]. Fermigier, M. and Gast, A.P., 1992, "Structure evolution in a paramagnetic latex suspension", Journal of Colloid and Interface Science. **154**(2): p. 522-539.
[42]. Claracq, J., Sarrazin, J., and Montfort, J.P., 2004, "Viscoelastic properties of magnetorheological fluids", Rheologica Acta. **43**(1): p. 38-49.
[43]. Ginder, J.M., 1998, "Behavior of magnetorheological fluids", Mrs Bulletin. **23**(8): p. 26-29.
[44]. Rosensweig, R.E., Kaiser, R., and Miskolczy, G., 1969, "Viscosity of magnetic fluid in a magnetic field", Journal of Colloid and Interface Science. **29**(4): p. 680-686.
[45]. Rosensweig, R.E., 1996, ""Negative viscosity" in a magnetic fluid", Science. **271**(5249): p. 614-615.
[46]. Rinaldi, C. and Zahn, M., 2002, "Effects of spin viscosity on ferrofluid duct flow profiles in alternating and rotating magnetic fields", Journal of Magnetism and Magnetic Materials. **252**(1-3): p. 172-175.
[47]. Zahn, M. and Pioch, L.L., 1999, "Ferrofluid flows in AC and traveling wave magnetic fields with effective positive, zero or negative dynamic viscosity", Journal of Magnetism and Magnetic Materials. **201**: p. 144-148.
[48]. Kordonsky, W.I., Demchuk, S. A., 1996, "Additional Magnetic Dispersed Phase Improves the MR-Fluid Properties", Journal of Intelligent Material Systems and Structures. **7**(5): p. 522-525.

[49]. Popplewell, J., Rosensweig, R.E., and Siller, J.K., 1995, "Magnetorheology of Ferrofluid Composites", Journal of Magnetism and Magnetic Materials. **149**(1-2): p. 53-56.
[50]. Kormann, C., Laun, H.M., and Richter, H.J., 1996, "MR fluids with nano-sized magnetic particles", International Journal of Modern Physics B. **10**(23-24): p. 3167-3172.
[51]. Chin, B.D., Park, J.H., Kwon, M.H., and Park, O.O., 2001, "Rheological properties and dispersion stability of magnetorheological (MR) suspensions", Rheologica Acta. **40**(3): p. 211-219.
[52]. Poddar, P., Wilson, J.L., Srikanth, H., Yoo, J.H., Wereley, N.M., Kotha, S., Barghouty, L., and Radhakrishnan, R., 2004, "Nanocomposite magneto-rheological fluids with uniformly dispersed Fe nanoparticles", Journal of Nanoscience and Nanotechnology. **4**(1-2): p. 192-196.
[53]. Phule PP, G.J., 1999, "Synthesis and properties for novel magnetorheological fluids having improved stability and re-dispersibility", Int. J Mod Phys B. **12**: p. 2019-2027.
[54]. Chen ZY, T.X., Zhang GC, Lin Y, Ni W, Zhu YR, "A novel approach of preparing ultra fine magnetic metallic particles and magnetorheology measurements for suspensions containing these particles" *Electro-rheological fluids, Magneto-rheological suspensions and their applications*, N.M.K. K, Editor. 1998, World Scientific: Singapore.
[55]. Deshmukh, S., Ph.D Thesis, 2006
[56]. Yang, Y., Grulke, E.A., Zhang, Z.G., and Wu, G.F., 2005, "Rheological behavior of carbon nanotube and graphite nanoparticle dispersions", Journal of Nanoscience and Nanotechnology. **5**(4): p. 571-579.
[57]. Eastman, J.A., Phillpot, S.R., Choi, S.U.S., and Keblinski, P., 2004, "Thermal transport in nanofluids", Annual Review of Materials Research. **34**: p. 219-246.
[58]. Olle, B., Bucak, S., Holmes, T.C., Bromberg, L., Hatton, T.A., and Wang, D.I.C., 2006, "Enhancement of oxygen mass transfer using functionalized magnetic nanoparticles", Industrial & Engineering Chemistry Research. **45**(12): p. 4355-4363.
[59]. Wang, X.W., Xu, X.F., and Choi, S.U.S., 1999, "Thermal conductivity of nanoparticle-fluid mixture", Journal of Thermophysics and Heat Transfer. **13**(4): p. 474-480.
[60]. Evans, W., Fish, J., and Keblinski, P., 2006, "Role of Brownian motion hydrodynamics on nanofluid thermal conductivity", Applied Physics Letters. **88**(9).
[61]. Choi, S.U.S., Zhang, Z.G., Yu, W., Lockwood, F.E., and Grulke, E.A., 2001, "Anomalous thermal conductivity enhancement in nanotube suspensions", Applied Physics Letters. **79**(14): p. 2252-2254.
[62]. Keblinski, P., Phillpot, S.R., Choi, S.U.S., and Eastman, J.A., 2002, "Mechanisms of heat flow in suspensions of nano-sized particles (nanofluids)", International Journal of Heat and Mass Transfer. **45**(4): p. 855-863.
[63]. Einstein, A., *Investigations on the Theory of the Brownian Movement.* 1985, New York: Dover.

[64]. Buongiorno, J., 2006, "Convective transport in nanofluids", Journal of Heat Transfer-Transactions of the Asme. **128**(3): p. 240-250.
[65]. Kim, J.K., Jung, J.Y., and Kang, Y.T., 2006, "The effect of nano-particles on the bubble absorption performance in a binary nanofluid", International Journal of Refrigeration-Revue Internationale Du Froid. **29**(1): p. 22-29.
[66]. Kim, S.D. and Kang, Y., 1997, "Heat and mass transfer in three-phase fluidized-bed reactors - an overview", Chemical Engineering Science. **52**(21-22): p. 3639-3660.
[67]. Brilman, D.W.F., Goldschmidt, M.J.V., Versteeg, G.F., and van Swaaij, W.P.M., 2000, "Heterogeneous mass transfer models for gas absorption in multiphase systems", Chemical Engineering Science. **55**(15): p. 2793-2812.
[68]. Dumont, E. and Delmas, H., 2003, "Mass transfer enhancement of gas absorption in oil-in-water systems: a review", Chemical Engineering and Processing. **42**(6): p. 419-438.
[69]. Zhang, G.D., Cai, W.F., Xu, C.J., and Zhou, M., 2006, "A general enhancement factor model of the physical absorption of gases in multiphase systems", Chemical Engineering Science. **61**(2): p. 558-568.
[70]. Chen, C.M. and Leu, L.P., 2001, "A highly elevated mass transfer rate process for three-phase, liquid-continuous fluidized beds", Chemical Engineering Journal. **81**(1-3): p. 223-230.
[71]. Ali, A., Vafai, K., and Khaled, A.R.A., 2004, "Analysis of heat and mass transfer between air and falling film in a cross flow configuration", International Journal of Heat and Mass Transfer. **47**(4): p. 743-755.
[72]. Xie, H.Q., Lee, H., Youn, W., and Choi, M., 2003, "Nanofluids containing multiwalled carbon nanotubes and their enhanced thermal conductivities", Journal of Applied Physics. **94**(8): p. 4967-4971.
[73]. Lee, S., Choi, S.U.S., Li, S., and Eastman, J.A., 1999, "Measuring thermal conductivity of fluids containing oxide nanoparticles", Journal of Heat Transfer-Transactions of the Asme. **121**(2): p. 280-289.
[74]. Krishnamurthy, S., Bhattacharya, P., Phelan, P.E., and Prasher, R.S., 2006, "Enhanced mass transport in nanofluids", Nano Letters. **6**(3): p. 419-423.
[75]. Jang, S.P. and Choi, S.U.S., 2004, "Role of Brownian motion in the enhanced thermal conductivity of nanofluids", Applied Physics Letters. **84**(21): p. 4316-4318.
[76]. Taylor, G.I., 1953, "Dispersion of soluble matter in solvent flowing slowly through a tube", Proceedings of the Royal Society A. **219**: p. 186-203.
[77]. Aris, R., 1956, "On the dispersion of a solute in a fluid flowing through a tube", Proceedings of the Royal Society. **235**: p. 67-77.
[78]. Samouhos, S.V. and McKinley, G.H., 2006, "Carbon Nanotube-Magnetite Composites, with applications to developing unique magnetorheological fluids", ASME Journal of Fluids Engineering. **129**.